Acta Pharmaceutica Sinica B 2026;16(7):4616−4633

Chinese Pharmaceutical Association
Institute of Materia Medica, Chinese Academy of Medical Sciences

Acta Pharmaceutica Sinica B

www.elsevier.com/locate/apsb
www.sciencedirect.com

ORIGINAL ARTICLE

Engineering an immuno-nanoprodrug: Photo-controlled pyroptosis synergizing with acid-activatable immunometabolic blockade for potent cancer immunotherapy

Zhiliang Yu[a,†], Hong Wang[b,†], Qin Yu[a], Fengze Miao[a], Rongrong Chai[a], Zongguang Tai[a,*], Zhongjian Chen[a,*], Quangang Zhu[a,*]

[a]*Shanghai Skin Disease Hospital, Shanghai Engineering Research Center for Topical Chinese Medicine, School of Medicine, Tongji University, Shanghai 200443, China*
[b]*Research Center for Translational Medicine at East Hospital, School of Life Science and Technology, Tongji University, Shanghai 200092, China*

Received 8 September 2025; received in revised form 22 October 2025; accepted 18 November 2025

KEY WORDS

Immuno-nanoprodrug;
Immunometabolic blockade;
Pyroptosis induction;
Adenosine−A2AR;
Photo-controlled;
Acid-activatable;
Cancer immunotherapy;
Photoimmunotherapy

Abstract Although immunotherapy has revolutionized cancer treatment, antitumor immunological responses remain limited by insufficient tumor immunogenicity and immunosuppressive tumor microenvironment. Herein, pyroptosis induction is integrated into a photosensitizer to potentiate tumor immunogenicity. In this part, artesunate is disclosed to increase GSDME and modified to synthesize its ROS-cleavable prodrug, which is then installed into the self-assembled photosensitizer, resulting in a novel oil-in-water nanoplatform (BDP-pATS). The cytotoxicity, pyroptosis feature and potentiated GSDME induced by BDP-pATS are well confirmed. Subsequently, a novel acid-activatable adenosine−A2AR inhibitor is synthesized and further installed into the aforementioned platform to obtain BDP-pATS-aA2Ai, manipulating immunometabolic strategy to counterbalance the enhanced adenosine caused by pyroptosis. Such a photo-controlled and acid-activatable nanoprodrug enhances cytotoxic T cell functions while restrains regulatory T cell activities, leading to potent effects toward primary and abscopal tumor inhibition. In addition, BDP-pATS-aA2Ai also manifests desirable performance on pulmonary metastasis and tumor recurrence mouse model. To the best of our knowledge, this study presents the first concept of blocking adenosine−A2AR pathway during pyroptosis occurrence. Collectively, this work strategically combines

*Corresponding authors.
E-mail addresses: taizongguang@126.com (Zongguang Tai), aajian818@163.com (Zhongjian Chen), qgzhu@126.com (Quangang Zhu).
†These authors made equal contributions to this work.
Peer review under the responsibility of Chinese Pharmaceutical Association and Institute of Materia Medica, Chinese Academy of Medical Sciences.

https://doi.org/10.1016/j.apsb.2026.01.024

immunometabolic interception, pyroptosis induction, photodynamic therapy and epigenetic regulation, emphasizing the significance of comprehensive therapy, which should open up a new viewpoint for cancer immunotherapy.

1. Introduction

Cancer immunotherapy has emerged as a remarkable therapeutic paradigm that stimulates the host immune system against primary and metastatic tumor recurrence[1−4]. However, up to now, only a small subset of patients can benefit from mono- or combined-immunotherapy with limited clinical response[5−9]. Growing evidence has indicated that antitumor responses primed by current immunotherapies are restricted by insufficient tumor immunogenicity and immunosuppressive tumor microenvironment (TME)[10−12]. Consequently, discovery of novel approaches, particularly comprehensive strategies capable of enhancing tumor immunogenicity while counteracting immune escape, would be highly desirable[13,14].

Pyroptosis was identified as a novel programmed cell death pattern, characterized by cell morphology swelling, plasma membrane rupture and release of inflammatory cytokines, ultimately enhancing tumor immunogenicity and further stimulating the host potent immune response[15−20]. Currently, reactive oxygen species (ROS) produced by some chemotherapy drugs are related with transforming tumor cells from apoptosis to certain pyroptosis[21]. Featured by ROS-dependent therapeutic platform, photodynamic therapy (PDT) employs photosensitizers to generate ROS to kill tumor cells[22]. Unfortunately, noninflammatory apoptosis is a significant cell death manner during PDT, making its triggered antitumor immunity not sufficiently potent[23−25]. Apoptosis is mainly mediated by caspase-3/-7 activation, while classical pyroptosis involves caspase-1/-4/-5/-11. Recent findings identified that caspase-3-mediated cell death can effectively trigger pyroptosis *via* gasdermin-E (GSDME) activation, linking the apoptotic and pyroptotic pathways[26,27]. However, lower GSDME expression caused by hypermethylation in many tumor cells limits the occurrence of pyroptosis when caspase-3 is activated[28]. Recently, DNA methyltransferase inhibitors (DNMTi) were reported to increase GSDME expression in tumor cells, transforming noninflammatory apoptosis to pro-inflammatory pyroptosis[26]. Inspired by these findings, PDT-triggered pyroptosis was attempted through combination of photosensitizer with DNMTi.

Currently, only two FDA-approved drugs were used as DNMTi, namely decitabine and azacitidine, both with very similar cytidine chemical structure[29,30]. However, previous work has indicated that decitabine faced a dilemma of simultaneously curing and inducing tumor even at nanomolar concentrations, *via* hypomethylated mechanism towards both tumor-suppressor genes and oncogene[31]. Very recently, DNMTi with thiol-substituted cytidine analogs was reported to result in lymphoid leukemia, which should confine its systematic application[32]. Pioneered works mainly manipulated decitabine as DNMTi to increase GSDME, with work concentration up to several micromolar level, which may further aggravate the side effects of decitabine[28,33]. In this work, we disclosed for the first time that artesunate can serve as a chemical drug to increase GSDME level, with only nanomole concentration and favorable performance. Furthermore, nonselective pyroptosis is a significant cause of toxic side effects produced by chemotherapeutic agents, emphasizing the importance of precise and controllable regulation of pyroptosis[28,34,35]. To potentiate the precise release efficiency of drugs, endogenous stimuli such as tumor-enriched reductive species and enzymes as well as lower pH values were widely used in drug design. Compared with these modes, photo-controlled drug released pattern attracts considerable attention recently, with merits of not only safety and highly spatiotemporal resolution, but also decreasing the off-target adverse effects[36−40]. Herein, an artesunate prodrug was chemically synthesized *via* ROS-cleavable thioketal linker[41,42], unleashing artesunate upon reaction with ROS generated from chemical drugs (*e.g.*, photosensitizer), which decreased the possible systemic toxicity caused by artesunate upon *in vivo* circulation. In addition, from the perspective of drug delivery, currently reported works primarily need the assistance of delivery vectors or surfactants, resulting in complicated architecture or undesirable toxicity upon systemic delivery[43,44]. In this design, we converted our previously reported carboxyl-functionalized BODIPY photosensitizer into its sodium salt form, which simultaneously served as both a surfactant-free drug delivery vector and an effective PDT agent[24,45,46]. Artesunate prodrug (pATS) was then installed into the oil-phase core surrounded by BODIPY salt *via* self-assembly, resulting in a novel oil-in-water nanoplatform (named as BDP-pATS) with convenient preparation process. After being taken up by cells, ROS generated from photosensitizer upon irradiation can cleave pATS to form artesunate (ATS), followed by increasing GSDME and subsequent pyroptotic occurrence, thereby achieving photo-controlled pyroptosis with high spatiotemporal selectivity.

As every coin has two sides, pyroptosis is also a double-edged sword[28]. The release of large amounts of ATP, an immune-activating molecule, is considered a hallmark of pyroptosis. Besides, due to tumor microenvironment features such as hypoxia, inflammatory reaction and nutrient deprivation, extracellular ATP in TME is noticeable higher than that in normal tissues. However, ectoenzymes of CD39 and CD73 acting in concert can catabolize ATP into adenosine, which then interacts with A2A receptor (A2AR) on immune cells, such as T lymphocytes, dendritic cells (DCs), macrophages and natural killer (NK) cells, ultimately tipping the balance from an immunostimulatory to an immunosuppressive microenvironment[47,48]. Recently, immunometabolic cancer therapy has emerged as an attractive strategy for TME intervention, wherein adenosine−A2AR pathway represents a novel promising next-generation immune checkpoint against malignancies[1,49−54]. Consequently, combining pyroptosis occurrence and adenosine−A2AR pathway interception should be a promising strategy, which within our scope of knowledge, has not yet been investigated up to now. Furthermore, as adenosine receptors are widely expressed in various human tissues, precise

release of adenosine−A2AR antagonists is particularly needed as the concern of immune-related adverse events. Unfortunately, TME stimulate-activable adenosine−A2AR antagonists are also not yet attempted so far. Inspired by these facts, we herein for the first time chemically synthesized an acid-activatable A2AR antagonist prodrug (aA2Ai), and further incorporated it into the oil-phase core surrounded by BODIPY salt *via* self-assembly and named the obtained nanoprodrug as BDP-pATS-aA2Ai. As illustrated in Scheme 1, the well-designed BDP-pATS-aA2Ai has four merits: 1) photo-controlled pyroptosis enables spatiotemporally precise regulation, amplifying the immunotherapeutic efficacy of PDT against both abscopal and recurrent tumors; 2) acid-activable A2AR inhibitor precisely intercept adenosine−A2AR pathway in TME; 3) normal tissues are free of photo- or acid-activatable, thus significantly reducing off-target effects; 4) the surfactant-free photosensitizer served as a self-delivering drug carrier system, which decreased the side effects and simplified the preparation process.

Taken together, we leverage the potential of photo-controlled pyroptosis to potentiate *in situ* tumor immunogenicity, and simultaneously fight against immunosuppressive TME *via* blocking immunometabolic using TME acid-activatable A2AR antagonist. The cytotoxicity, photo-triggered pyroptosis efficacy and potentiated GSDME level induced by BDP-pATS were well manifested. Subsequently, the *in vivo* efficacy against primary and bilateral tumor on living mouse model using BDP-pATS-aA2Ai was further testified, as evidenced by increased mature DC, T lymphocytes infiltration, and restrained regulatory T cells activities. Furthermore, BDP-pATS-aA2Ai also achieved potent effects on lung metastasis and tumor recurrence on living mouse model. Such an integrated nanotherapeutic platform synergistically combined immunometabolic modulation, pyroptosis induction, photodynamic therapy, and epigenetic regulation, demonstrating the critical need for adenosine−A2AR pathway blockade during pyroptosis, ultimately enabling spatiotemporally optimized cancer immunotherapy.

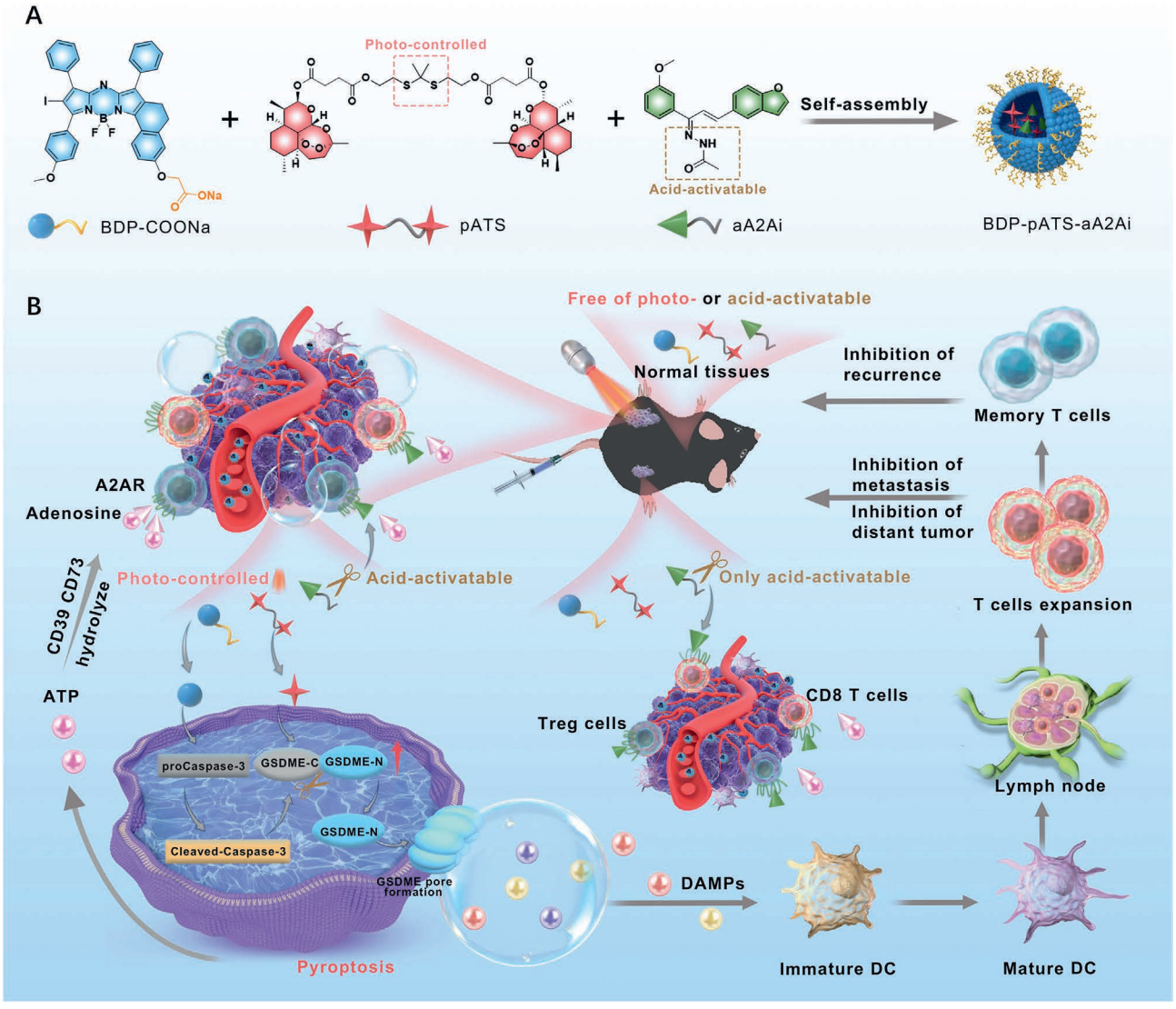

Scheme 1 (A) Preparation of BDP-pATS-aA2Ai nanoprodrug. (B) Schematic diagram of synergistic immunotherapy based on BDP-pATS-aA2Ai evoked photo-controlled pyroptosis occurrence and acid-activatable adenosine−A2AR pathway blocking. The figure was created with BioRender.com.

2. Materials and methods

2.1. Chemicals and reagents

All chemicals and solvents were purchased from Sigma-Aldrich and Sinopharm Chemical Reagent and used directly. TLC detection was performed on silica gel GF254 plates and column chromatography was carried out using 200−300 mesh silica gel. ^{1}H NMR spectra were finished on a Bruker Avance IV 600 MHz spectrometer. ^{13}C NMR spectra were measured on a Bruker Avance IV 151 MHz spectrometer. The chemical shifts (δ) were reported in ppm (parts per million) using tetramethylsilane as the interior label. Coupling constants (J) were measured in hertz (Hz).

H_2DCFDA was purchased from Molecular Probes. Rabbit anti-HMGB1 antibody, Alexa Fluor 488-labeled goat anti-rabbit secondary antibody, caspase-3 activity assay kit, LDH detection kit and ATP detection kit were purchased from Beyotime Biotechnology. Collagenase type 1 and collagenase type 4 were purchased from Rockland Immunochemicals. TGF-β ELISA kit, IL-10 ELISA kit, FITC anti-mouse CD80, PE anti-mouse CD86, APC anti-mouse CD45, FITC anti-mouse CD4, PE anti-mouse CD8, APC anti-mouse CD25, PE anti-mouse Foxp3 were purchased from Biolegend.

2.2. Chemical synthesis procedure of pATS, A2Ai and aA2Ai

2.2.1. Synthesis of pATS

Artesunate (115.2 mg, 0.3 mmol) and ROS-cleavable linker (19.6 mg, 0.1 mmol) were dissolved in a solution of 5 mL dry DCM at 0 °C, then DCC (30.9 mg, 0.15 mmol) and DMAP (18.3 mg, 0.15 mmol) was added, followed by stirring for 24 h at room temperature. The reaction was monitored by TLC until completion, which was purified by column chromatography with CH_2Cl_2/MeOH (200/1) as the eluent to obtain the product pATS (76.3 mg, yield of 82.2%). ^{1}H NMR (600 MHz, $CDCl_3$) δ 5.79 (d, J = 8.0 Hz, 2H), 5.43 (s, 2H), 4.28 − 4.21 (m, 2H), 2.89 − 2.82 (m, 4H), 2.78 − 2.67 (m, 6H), 2.66 − 2.54 (m, 4H), 2.41 − 2.34 (m, 2H), 2.08 − 1.99 (m, 2H), 1.93 − 1.85 (m, 2H), 1.81 − 1.75 (m, 2H), 1.74 − 1.70 (m, 2H), 1.63 (dd, J = 8.3, 3.8 Hz, 2H), 1.61 (s, 6H), 1.53 − 1.46 (m, 2H), 1.43 (s, 6H), 1.40 − 1.31 (m, 4H), 1.29 − 1.24 (m, 2H), 1.05 − 0.99 (m, 2H), 0.96 (d, J = 6.1 Hz, 6H), 0.86 (d, J = 7.1 Hz, 6H). ^{13}C NMR (151 MHz, $CDCl_3$) δ 171.86, 171.08, 104.47, 92.20, 91.52, 80.12, 63.74, 56.47, 53.44, 51.58, 45.25, 37.28, 36.23, 34.10, 31.82, 31.00, 29.16, 28.98, 28.78, 25.97, 24.59, 22.01, 20.22, 12.08.

2.2.2. Synthesis of A2Ai

A2Ai was obtained as the reported method[55]. ^{1}H NMR (600 MHz, $CDCl_3$) δ 7.94 (d, J = 15.6 Hz, 1H), 7.88 (d, J = 1.7 Hz, 1H), 7.67 (d, J = 2.2 Hz, 1H), 7.63 (ddd, J = 8.1, 4.5, 1.4 Hz, 2H), 7.57 (dd, J = 2.5, 1.6 Hz, 1H), 7.53 (t, J = 11.9 Hz, 2H), 7.42 (dd, J = 14.0, 6.1 Hz, 1H), 7.14 (ddd, J = 8.2, 2.7, 0.8 Hz, 1H), 6.82 (dd, J = 2.2, 0.9 Hz, 1H), 3.90 (s, 3H).

2.2.3. Synthesis of aA2Ai

Acethydrazide (74 mg, 1.0 mmol) was dissolved in 5 mL methanol, followed by addition of A2Ai (27.8 mg, 0.1 mmol) and trifluoroacetic acid (5 μL). The solution was stirred for 10 h at room temperature until completion, which was then purified by column chromatography using CH_2Cl_2/MeOH (300/1) to obtain the final product aA2Ai (29.5 mg, yield of 88.3%). ^{1}H NMR (600 MHz, $CDCl_3$) δ 8.28 (s, 1H), 7.61 (d, J = 2.0 Hz, 2H), 7.56 − 7.42 (m, 2H), 7.39 (dd, J = 8.6, 1.7 Hz, 1H), 7.09 (d, J = 16.3 Hz, 1H), 7.07 − 6.97 (m, 1H), 6.83 − 6.78 (m, 1H), 6.73 (ddd, J = 2.8, 2.3, 1.1 Hz, 2H), 6.51 (d, J = 16.3 Hz, 1H), 3.94 − 3.81 (m, 3H), 2.42 − 2.33 (m, 3H). ^{13}C NMR (151 MHz, $CDCl_3$) δ 172.61, 160.59, 155.20, 152.43, 145.80, 137.64, 132.05, 131.28, 131.06, 127.95, 127.35, 123.40, 120.33, 120.07, 115.38, 113.73, 111.70, 106.68, 55.43, 20.54.

2.3. Preparation of the BDP-pATS-aA2Ai nanoprodrug

The BDP-pATS-aA2Ai nanoparticles were prepared as a previously reported procedure with some modifications. Firstly, BDP reacted with NaOH to form its sodium salt BDP-COONa. BDP-COONa (3.1 mg), glyceryl trioctanoate (19.1 mg), pATS (0.6 mg) and aA2Ai (0.2 mg) were dissolved in a mixture of $CHCl_3$ (9 mL) and MeOH (1 mL), which is then dried using rotary evaporator to form thin film. PBS (6 mL) was added and the film was bath sonicated at 50 °C for 30 min, followed by passing through a microfluidizer (channel dimensions of 70 cm × 36 cm × 30 cm, flow rate of 120 mL/min) at 10,000 psi for 10 cycles. The obtained solution was further purified *via* centrifugation at 12,000 rpm for 1 h. The final concentration of BDP-pATS-aA2Ai was adjusted to 200 μmol/L by determining its contained BDP using UV−Vis spectrophotometer. The preparation protocol for BDP-pATS is identical to that of BDP-pATS-aA2Ai except the absence of aA2Ai. To assess drug encapsulation efficiency and loading capacity, high-performance liquid chromatography (HPLC) was used at 1 mL/min on a C18 column (Agilent 5 HC-C18, 250 mm × 4.6 mm). Compounds were first dissolved in tetrahydrofuran (THF)/CH_3CN (1/2, *v*/*v*) and pure CH_3CN was used as the mobile phase.

2.4. Cellular uptake assay

B16-F10 cells were seeded on the glass-bottom dishes at a density of 3 × 10^3 cells and allowed to adhere overnight. Afterwards, BDP-pATS (at BDP concentration of 250 nmol/L) and BDP (250 nmol/L) were added and incubated at indicated time points. Then, cells were washed with PBS twice and incubated with DAPI for 30 min, followed by detection using confocal laser scanning microscopy (CLSM) at 1, 3, 6 and 24 h.

2.5. Detection of the intracellular ROS level

B16-F10 cells were seeded on a six-well plate followed by incubating with various drugs (250 nmol/L) for 16 h, which was then placed at 37 °C in a humidified incubator. After being washed three times with PBS, the cells were then incubated with a ROS detecting probe H_2DCFDA in PBS (10 μmol/L, 100 μL) for 30 min in the incubator. The cells were then washed with PBS twice and supplied with fresh PBS, finally exposed to an LED irradiation for 10 min (680 nm, 2 mW/cm^2). The cells were then collected and determined immediately using flow cytometry.

2.6. Evaluation of cell viability

The incubated cells were adjusted to 3 × 10^3 cells per well and cultured for 24 h on a 96-well plate, which was incubated for 3 h with different drugs of various concentrations. After exposing to an LED light (680 nm, 2 mW/cm^2) at 3 h (3 min) and 24 h (7 min) respectively, the cells were further cultured for 24 h at 37 °C.

After removing the culture medium, a solution of 150 μL new cultured medium containing 10% CCK-8 was added and incubated for 2 h at 37 °C. Finally, the absorbance at 450 nm was detected using a Synergy H1 microplate reader. For dark toxicity, cell viability was evaluated as described above without irradiation.

2.7. Cell morphology observation and HMGB1 release detection

B16-F10 cells were incubated with indicated treatments and irradiated at 3 h (3 min) and 24 h (7 min) using an LED light (680 nm, 2 mW/cm^2), followed by incubating for another 6 h to observe cell morphology on CLSM. Meanwhile, cells with light irradiation were washed with PBS and fixed with 4% paraformaldehyde for 20 min, which was then permeabilized with 1% Triton X-100 for 20 min and blocked with the blocking solution for 1 h. The cells were washed with PBS and incubated with rabbit anti-HMGB1 antibody at 4 °C for 24 h, which was washed by cold PBS and treated with Alexa Fluor 488-labeled goat anti-rabbit secondary antibody at 25 °C for 1 h. Finally, the cells were incubated with DAPI at 25 °C for 5 min, followed by washing with PBS and imaging using CLSM.

2.8. SiRNA knockdown of GSDME

To knock down GSDME protein expression, B16-F10 cells were seeded in six-well plates at a density of 3×10^5 cells per well. Transfection of GSDME-targeting siRNAs (RiboBio) was performed using Lipofectamine 3000 transfection reagent in accordance with the manufacturer's protocol. After 48 h, the cells were subjected to the indicated treatments for subsequent experiments.

2.9. Determination of relative cleaved caspase-3, LDH and ATP levels

The relative cleaved caspase-3 level, released LDH and ATP levels of cells were detected using caspase-3 activity assay kit, LDH release assay kit, and ATP assay kit according to the manufactures' instruction, respectively.

2.10. Ex vivo fluorescence imaging

B16-F10 tumor-bearing mice were intravenously injected with BDP (100 μmol/L) or BDP-pATS (at BDP concentration of 100 μmol/L) *via* tail vein and imaged on an IVIS imaging equipment (PerkinElmer, Waltham, Massachusetts, USA) at 12, 24, 48 and 72 h. The excitation and emission wavelengths were set to 680 and 720 nm, respectively. At predetermined time, mice were first euthanized and heart, liver, spleen, lungs, kidneys, and tumors were excised, which were then placed on the black paper for *ex vivo* imaging using an IVIS imaging system. Fluorescence intensity was quantified using Living Image software (PerkinElmer). All results were collected as the mean ± standard deviation (SD).

2.11. Animals and tumor models

All animal experimental procedures were approved by the Animal Ethical Care and Use Committee of Tongji University (Protocol no.TJAA15424101). C57BL/6 mice bearing B16-F10 cells were used with tumor volumes of 90−110 mm^3 and body weights of 18−22 g. For primary tumor inoculation, 3×10^5 B16-F10 cells suspended in 0.1 mL PBS were injected subcutaneously into the right flank of the mice. Six days later (counted as Day 0), mice were randomly assigned to five groups and injected with PBS, ATS (1 mg/kg), BDP, BDP-pATS and BDP-pATS-aA2Ai *via* tail vein, respectively. For bilateral tumor inoculation, 3×10^5 B16-F10 cells suspended in 0.1 mL PBS were inoculated subcutaneously for both primary and distant tumors. For BDP-containing groups, the injection concentration of BDP was adjusted to 200 μmol/L by determining its content using UV−Vis spectrophotometer. For *in vivo* assays, a laser light (660 nm, light power of 200 mW/cm^2) was used with the first irradiation was 3 min and the second irradiation was 7 min. The long (L) and short (W) diameters of tumors, as well as body weights were collected every other day. The tumor volume (V) was calculated as following Eq. (1):

$$V = 0.5 \times \left(L \times W^2\right) \quad (1)$$

Kaplan−Meier survival curve was plotted according to the tumor volume of each mouse.

2.12. Histological analysis of tumors

As for H&E staining, tumors were fixed with 4% paraformaldehyde, dehydrated with graded alcohol, and finally embedded with paraffin, sectioned at 4 μm slices and stained with H&E before light-microscopy imaging.

2.13. Evaluation for antitumor immune responses

The tumors were collected after various treatments and processed to produce a single cell suspension for flow cytometry. Briefly, the tissues were cut up thoroughly, ground in a homogenizer and digested with collagenase type 1 and collagenase type 4 at 37 °C for 45 min with tubes agitated every 5 min. After treatment, the suspensions were filtered with a 70 μm nylon cell strainer, which was then collected and passed through a 40 μm nylon cell strainer, followed by washing twice with PBS to obtain the single cell suspension. Subsequently, the resulting homogenates were adjusted to a cell density of 1×10^6 cells/mL and transferred to a flow tube for staining. APC anti-mouse CD45, FITC anti-mouse CD4 and PE anti-mouse CD8 antibodies were used for T cells analysis. FITC anti-mouse CD80 and PE anti-mouse CD86 antibodies were used for DCs analysis. APC anti-mouse CD25 and PE anti-mouse Foxp3 antibodies were used for Treg cells analysis. To detect the level of TGF-β and IL-10, tumors were collected on Day 14 and analyzed using ELISA kits.

2.14. Effects against pulmonary metastasis and tumor rechallenge studies

In anti-pulmonary metastasis assay, 3×10^5 B16-F10 cells suspended in 0.1 mL PBS were inoculated subcutaneously into the right flank of the mice. BDP-pATS and BDP-pATS-aA2Ai were intravenously injected followed by twice PDT. The cured mice were reinoculated with 3×10^5 B16-F10 cells on Day 10 *via* the tail vein injection. On Day 24, the mice were sacrificed and lungs were collected for imaging and H&E staining.

In tumor rechallenge study, 3×10^5 B16-F10 cells suspended in 0.1 mL PBS were inoculated subcutaneously into the right flank of the mice. BDP-pATS-aA2Ai was intravenously injected followed by twice PDT. After treatment, the cured mice were

reinoculated with 2×10^5 B16-F10 cells subcutaneously on Day 16. The tumor volumes were recorded in the following days.

2.15. Statistical analysis

GraphPad Prism 9.5 was used for plotting and analyzing statistical significance. ChemDraw 21.0.0 was used for chemical structure presentation. FlowJo 10.8.1 software was used for flow cytometry analyses. Student's *t*-test was used to obtain statistical comparisons. Data were presented as mean ± standard deviation (SD). $P < 0.05$ was considered statistically significant.

3. Results and discussion

3.1. Identify artesunate as a novel chemical drug to up-regulate GSDME and synthesize its ROS-cleavable prodrug

Aberrant epigenetic alterations, such as DNA methylation and histone modifications, were known to be closely correlated with neoplastic oncogenesis and progression. To figure out the expression of GSDME in melanoma patients, representative microscopic images of immunohistochemical staining of GSDME in melanoma tissues and normal controls were listed *via* data from The Human Protein Atlas. As shown in Fig. 1A, melanoma tumors exhibit remarkably lower GSDME levels as compared to normal tissues. Furthermore, we determined the relative mRNA expression of *Gsdme* in normal cells (NIH3T3 and 293T) and tumor cells (B16-F10), with results demonstrating that B16-F10 cells express significantly lower *Gsdme* compared to these two normal cells (Fig. 1B). These results indicated that employing pharmacological demethylation towards GSDME may reinforce the therapeutic efficacy against melanoma.

Recent research reported that dihydroartemisinin can increase GSDME level in GSDME low-expressing tumor cells[56], we thus speculated that artesunate (ATS), bearing the same chemical mother core, may exhibit similar activity. Therefore, we attempted the assumption using artesunate in B16-F10 cells with relative mRNA expressions testified firstly. The results proved that the relative mRNA expressions of *Gsdme* were noticeably up-regulated, and displayed concentration and incubation time dependent manners (Fig. 1C), which prompted us for further testification. As shown in Fig. 1D, artesunate obviously up-regulated GSDME levels in B16-F10 cell when incubated at 24 h at a concentration of 400 nmol/L. Furthermore, when the incubation time was extended to 48 h, artesunate can still remarkably potentiate GSDME level even at a lower concentration of 200 nmol/L, which is far below than that of classical demethylation agent decitabine (generally 5 μmol/L). These combined results indicated artesunate can serve as a novel pharmacological tool to down-regulate methylation of GSDME, which has never been reported previously within our scope of knowledge.

However, artesunate exhibited cellular toxicities in both verified tumor and normal cells, even at lower concentrations (Fig. 1F and G). Worse still, as shown in Fig. 1H, it can lead to the increase of *Gsdme* in normal cell (NIH3T3), which may result in side effects to normal tissues. These undesirable results prompt us to develop new strategies to figure out the dilemma. Prodrug represents a canonical strategy to reduce chemical drug toxicity, wherein ROS-cleavable manner has proved to be an effective approach to highly increase selectivity. Herein, we employed this approach to synthesize a novel artesunate prodrug (pATS) using thioketal group as the ROS-sensitive linker (Fig. 1E). This linker was acquired as reported method using condensation reaction, followed by LAH reduction in anhydrous THF. The obtained ROS-cleavable thioketal linker was then reacted with artesunate to get pATS, which was then purified by column chromatography. The final product pATS was confirmed by ^{1}H NMR, MS ($[M+Na]^+$, *m/z* 951.38) and ^{13}C NMR spectra (Supporting Information Figs. S1−S3), demonstrating the successful synthesis of its structure. Afterward, cytotoxicity was assessed in B16-F10 and NIH3T3 cells, with results showing that pATS achieved substantially reduced toxicity compared with artesunate (Fig. 1F and G). Moreover, pATS did not induce upregulation of *Gsdme* in NIH3T3 cells, demonstrating enhanced safety for normal cells compared to ATS (Fig. 1H). These results demonstrated that pATS effectively reduced cellular toxicity without altering *Gsdme* expression in normal cells, indicating that it can serve as a novel ROS-cleavable prodrug to up-regulate GSDME level.

3.2. Preparation and characterization of the BDP-pATS nanoagent

We previously reported that water-soluble BODIPY photosensitizers have obvious merits such as high light toxicity, low dark toxicity, easy preparation and favorable water solubility[24]. Herein, the mono-carboxyl BODIPY (named as B159) was selected to obtain its sodium salt BDP-COONa (named as BDP for abbreviation), which can serve as a surfactant-free drug delivery vector and simultaneously as a potent PDT agent. For the synthesis (Fig. 2A), material M1 was obtained as we previously reported method, which was then reacted with *tert*-butyl bromoacetate and K_2CO_3 in DMF to obtain M2 in 82.3% yield. The resulting M2 was treated with a solution of TFA/DCM to remove the *tert*-butyl protecting group, followed by halogenation with NIS in DCM/AcOH to form photosensitizer B159 in 66.8% yield. B159 was then reacted with NaOH in DMF, which was further added dropwise into water to yield its salt with a yield of 22.6%.

BDP bears amphiphilicity because of its hydrophobic aromatic ring and hydrophilic carboxylic acid salt, granting its affinity to the water−oil interface of lipid nanoparticles. Glyceryl trioctanoate, containing a molecular structure as that of the food fat extensively used in food grade emulsions, was applied as the oil phase to dissolve hydrophobic pATS. As shown in Fig. 2B, BDP-pATS was prepared by conveniently hydrating the film consisting of BDP, pATS and glyceryl trioctanoate, finally forming an oil-in-water microemulsion nanoagent *via* microfluidic processing[44,57]. Afterwards, dynamic light scattering (DLS) assay (Fig. 2C) showing that BDP-pATS revealed a *Z*-average of 138.1 ± 0.9 nm (PDI = 0.219 ± 0.008), which is further testified by transmission electronic microscopy (TEM) imaging displaying a monodispersed spherical structure (Fig. 2D). The drug-loading capacity and entrapment efficiency were determined to be 5.85 ± 0.21% and 76.6 ± 4.3%, respectively. Besides, the stability of BDP-pATS was also evaluated, it remained stable at 4 °C within 30 days (Fig. 2E and F).

3.3. Investigation of BDP-pATS towards cellular behaviors

To investigate the cellular behavior of BDP-pATS, the cell uptake ability was evaluated in B16-F10 cell using confocal laser scanning microscope (CLSM), and BDP with no formulation modification was also evaluated for comparison. Overall, as shown in Fig. 3A and Supporting Information Fig. S4, compared with

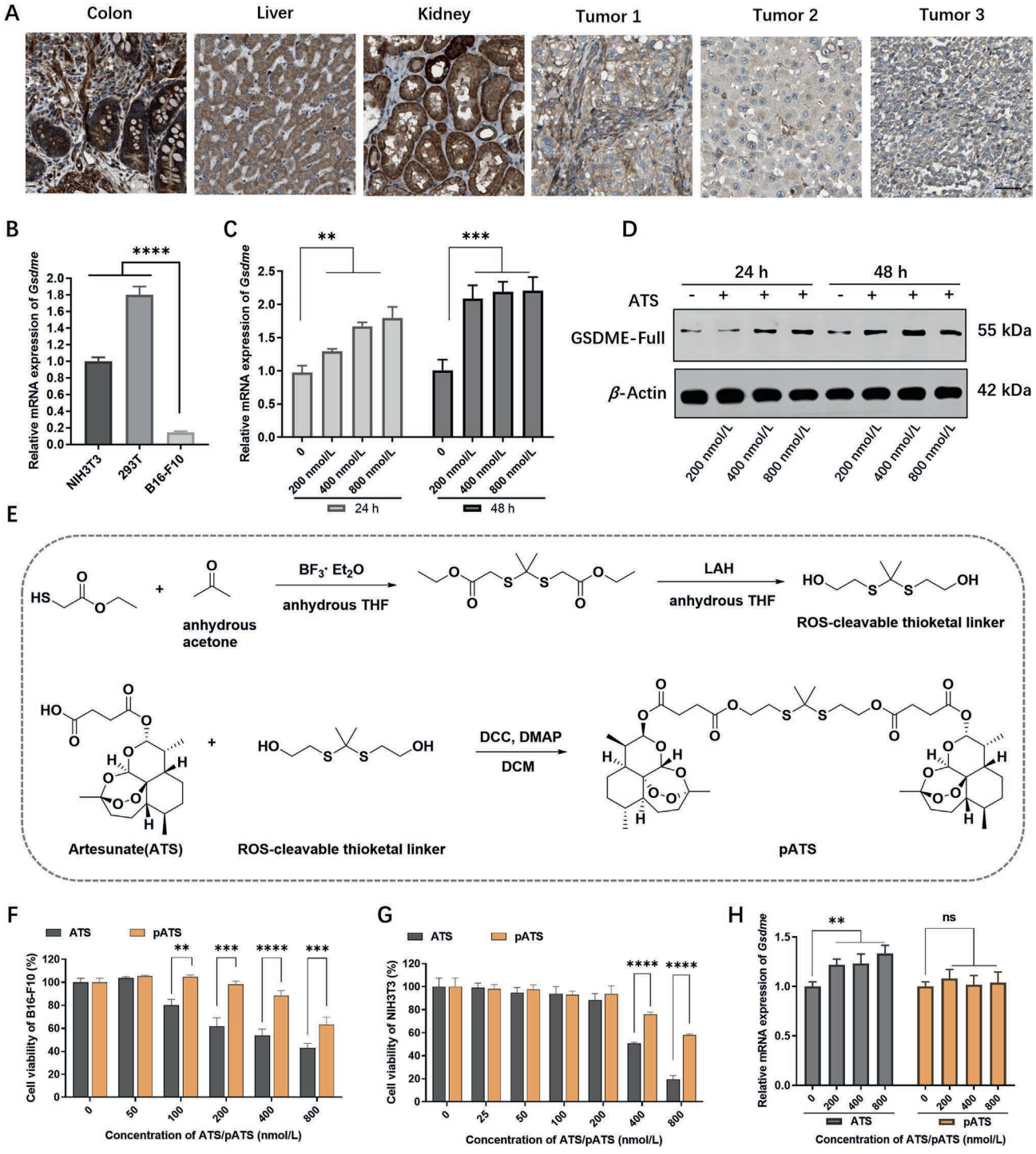

Figure 1 Identify artesunate (ATS) as a new chemical drug toward increasing GSDME level and synthesize its ROS-cleavable prodrug. (A) Representative microscopic images of immunohistochemical staining of GSDME in melanoma tissues and normal controls. The images were provided by The Human Protein Atlas (www.proteinatlas.org). Scale bar = 50 μm. (B) Relative mRNA expression of *Gsdme* in tumor cells (B16-F10) and normal cells (NIH3T3 and 293T). (C) Relative mRNA expression of *Gsdme* in B16-F10 cells when treated with ATS at varied concentrations and incubation times. (D) The effects of ATS on increasing GSDME levels using different concentrations after incubation for 24 and 48 h, respectively. (E) The synthetic route of pATS using ROS-cleavable thioketal linker. (F, G) Cell viabilities of ATS and pATS toward B16-F10 and NIH3T3 cells. (H) Relative mRNA expression of *Gsdme* in NIH3T3 cells when treated with ATS or pATS with varied concentrations for 24 h. Data are expressed as mean ± SD ($n = 3$). $^{**}P < 0.01$, $^{***}P < 0.001$, $^{****}P < 0.0001$ *vs*. indicated, and ns represents no significant difference.

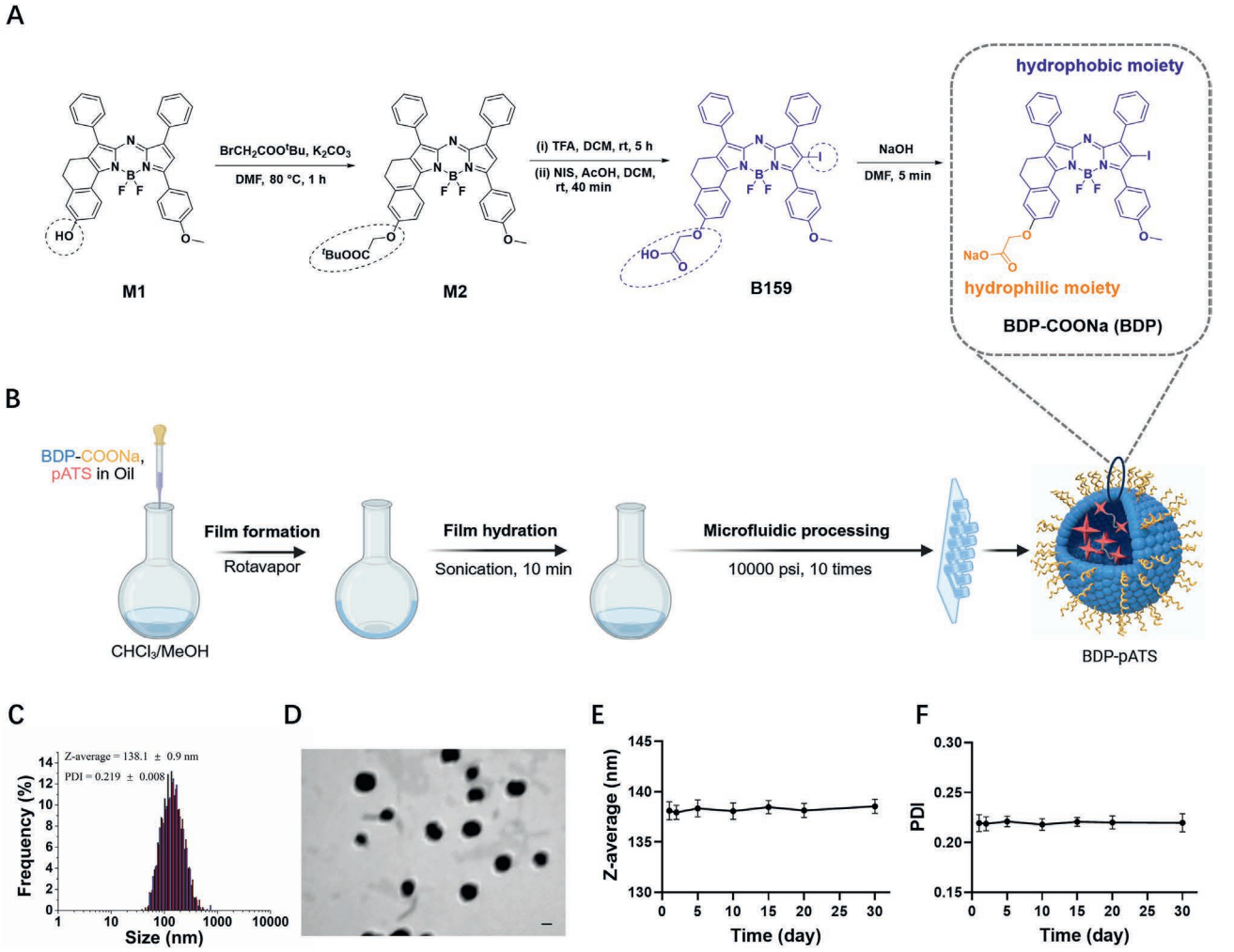

Figure 2 Preparation and characterization of BDP-pATS nanoagent. (A) Synthesis route of BDP-COONa. (B) Schematic preparation process of BDP-pATS. (C) The DLS composite spectra obtained from three independent replicate experiments of BDP-pATS: *Z*-average = 138.1 ± 0.9 nm; PDI = 0.219 ± 0.008. (D) TEM images of BDP-pATS. Scale bar = 100 nm. (E, F) *Z*-average sizes and PDI values of BDP-pATS within 30 days. Data are expressed as mean ± SD (n = 3).

BDP, BDP-pATS exhibited visually higher fluorescence intensity at each investigated time. As incubation time increased, the fluorescence intensity was also enhanced with maximum value at 24 h. Meanwhile, the relative intensities of corresponding red fluorescence in Fig. 3A were provided in Fig. 3C. Besides, ROS producing level is a critical parameter to evaluate PDT efficacy. Therefore, the ROS generation ability at the cellular level was firstly measured by flow cytometry. H_2DCFDA was used as the ROS fluorescent indicator, which can be hydrolyzed by intracellular enzyme to form non-fluorescent H_2DCF and further oxidized by intracellular ROS to generate fluorescent DCF. As shown in Fig. 3B, BDP-pATS displayed higher fluorescent intensity than BDP group, whereas both ATS and PBS groups revealed negligible fluorescent intensities.

As BDP-pATS is a precisely photo-controlled nanoagent, pATS can not be cleaved until reacted with ROS. Therefore, in this work a two-time-irradiated pattern was adopted, with the first irradiation to release ATS and the second irradiation to trigger pyroptosis. Subsequently, the cell viability was evaluated with or without light irradiation in B16-F10 cells. As shown in Fig. 3D, when no light was added, BDP displayed totally no toxicity, and BDP-pATS revealed only marginal cellular toxicity at the concentration of 2 μmol/L. The possible reason can be attributed to the significantly enhanced cellular uptake of BDP-pATS, causing its slightly increased dark toxicity. When light was added, as shown in Fig. 3E, BDP-pATS and BDP demonstrated potent dose-dependent light toxicity, with IC_{50} values of 208.7 and 647.3 nmol/L, respectively. It should be noted that such a result is obtained under an ultralow LED light irradiation (680 nm, 2 mW/cm^2, totally 10 min), which is convenient compared with highly heat-producing halogen lamp. Besides, ATS displayed unbiased toxicity whether light is existed, indicating light has little effects towards its cellular killing.

During the occurrence of pyroptosis, cellular morphology is considered as a canonical character, as evidenced by features such as cell swelling and production of large bubbles. Hence, the cell morphology was observed using CLSM. As displayed in Fig. 3F, numerous cells in BDP-pATS group showed cell swelling and large bubbles after 6 h of light irradiation. By contrast, no visually cellular morphology in BDP group displayed pyroptosis features, with only some apoptotic feature such as cell shrinkage. Besides, the cell morphology in control and other groups were also not

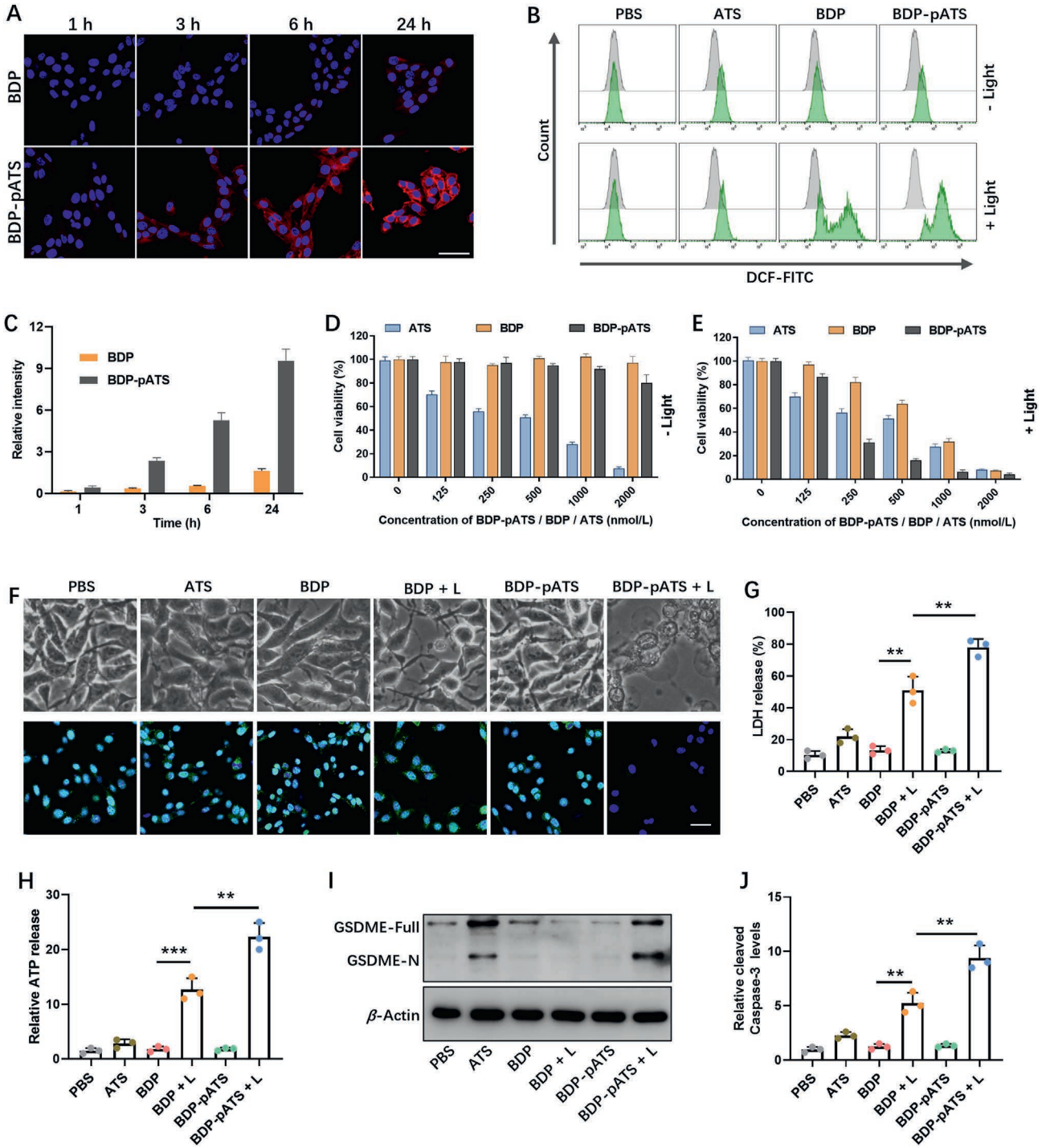

Figure 3 Investigation of BDP-pATS toward cellular behaviors. (A) Investigation of uptake behavior in B16-F10 cell using CLSM. Scale bar = 50 μm. (B) ROS generation evaluation determined by flow cytometry after irradiation. (C) Relative intensity of corresponding red fluorescence in (A). (D, E) Cell viability under dark or light conditions. (F) The cellular morphology changes (upper) and HMGB1 release behavior (lower) after irradiation. Green represents HMGB1 and blue shows DAPI. Scale bar = 20 μm. (G, H) Determination of LDH and ATP levels in extracellular supernatant. (I, J) GSDME-Full, GSDME-N and relative cleaved caspase-3 expression after light irradiation. ATS: 250 nmol/L; for BDP-containing groups, the working concentration of BDP was adjusted to 250 nmol/L by determining its content using UV−Visible spectrophotometer. An ultralow LED light (680 nm) was used for irradiation with light power of 2 mW/cm^2 for a total of 10 min (for assays of E−J, the first irradiation was 3 min, and 24 h later the second irradiation was given for 7 min). Data are expressed as mean ± SD ($n = 3$). $^{**}P < 0.01$ and $^{***}P < 0.001$ *vs*. indicated.

obviously altered. Furthermore, the occurrence of pyroptosis ignite large amount of intracellular contents leakage, such as typical markers of high-mobility group box 1 (HMGB1), lactate dehydrogenase (LDH) and adenosine triphosphate (ATP), which thus were evaluated by CLSM (for HMGB1) or detecting the cell supernatant (for LDH and ATP) of each group. As displayed in Fig. 3F, BDP-pATS + L group showed the lowest green (HMGB1) color, namely the most released HMGB1 from the nucleus, which correlated well with its damaged cellular morphology. As revealed in Fig. 3G, BDP-pATS + L group displayed the most potent LDH levels, which was 2.52- and 1.53-fold than that in control and BDP + L groups, respectively. Similarly, BDP-pATS + L group also exhibited the highest ATP release, which was 14.9- and 1.77-fold than that in control and BDP + L groups, respectively (Fig. 3H). Subsequently, GSDME knockdown in B16-F10 cells was also performed to investigate pyroptotic phenotypes changes. As displayed in Supporting Information Fig. S5A, GSDME knockdown resulted in significantly attenuated cell swelling and HMGB1 release after BDP-pATS + L treatment. Moreover, significantly decreased LDH and ATP release levels were observed in BDP-pATS + L group after GSDME knockdown (Fig. S5B and S5C). These combined results provide direct evidence that GSDME is required for the observed effects.

To investigate whether the occurrence of pyroptosis was mediated by the caspase-3/GSDME pathway, we subsequently detect GSDME-Full, GSDME-N and relative cleaved caspase-3 levels with various treatments followed by exposing to light irradiation. As shown in Fig. 3I, both ATS and BDP-pATS + L groups displayed enhanced GSDME-Full levels compared with control and other groups. Especially, BDP-pATS + L group verified the most potent GSDME-N level, followed by ATS group of slight GSDME-N and other groups of lower levels. In addition, relative cleaved caspase-3 levels were also determined, wherein groups of BDP-pATS + L and BDP + L induced potent results compared with other groups (Fig. 3J). Collectively, these results verified BDP-pATS could significantly trigger pyroptosis after exposing to light irradiation.

3.4. Preparation and characterization of BDP-pATS-aA2Ai nanoprodrug

During the occurrence of pyroptosis, large amount of ATP is released into the tumor environment, which is then hydrolyzed by extracellular CD39 and CD73 enzymes to form immunosuppressive adenosine. Finally, these adenosine binds with widespread A2A receptors (A2AR) on immune cells such as T lymphocytes, macrophages and NK cells et al., ultimately leading to immune escape (Fig. 4A). As shown in Fig. 4B and C, we therefore detected the adenosine levels in the supernatant of B16-F10 cells and tumor tissues, with maximum values at 8 h in cells and 12 h in tumor tissues post irradiation (BDP of 250 nmol/L as the photosensitizer: an LED light of 680 nm with light power of 2 mW/cm^2, 10 min for the cells; a laser light of 660 nm with light power of 200 mW/cm^2, 10 min for the tumors), respectively. Of note, all the determined results were significantly higher than control groups (B16-F10 cells or normal tissues). Unfortunately, up to now, few works have been investigated towards the effects of inhibiting A2AR−adenosine pathway during the occurrence of pyroptosis. Moreover, as A2AR is widely distributed in various tissues, development of precious released A2AR inhibitor is of particular significance.

Herein, we utilized the TME acid-activatable approach, a classical strategy applied in FDA-approved ADC prodrugs, to chemically modify a novel A2AR inhibitor[55,58-61]. Briefly, formation of acid-activatable hydrazone prodrug (aA2Ai) was achieved by reaction of acethydrazide and a recently reported A2AR inhibitor using TFA as the catalyst (Fig. 4D). The products of A2Ai and its hydrazone prodrug aA2Ai were identified by ^{1}H NMR and ^{13}C NMR spectra (Supporting Information Figs. S6−S8), demonstrating the successful synthesis of their structures. Afterwards, we examined the released behavior of aA2Ai at different pH values of 5.5, 6.5 and 7.4, respectively. As illustrated in Fig. 4E, release of A2Ai displayed a pH-dependent manner in aA2Ai solution, demonstrating higher release rate at lower pH values. At pH value of 5.5, aA2Ai was quickly hydrolyzed to A2AR inhibitor, with release rates over than 60% at 2 h and 90% at 12 h, respectively. However, at pH value of 7.4 which represents that of normal tissues, aA2Ai was stable with approximately 15% release rate at 12 h. These results indicated that aA2Ai can serve as an excellent A2Ai prodrug with precise acid-activatable property.

Encouraged by these aforementioned results, we attempted to incorporate aA2Ai prodrug into our constructed nanotherapeutic platform, aiming to counterbalance the adenosine-induced immunosuppression. As shown in Fig. 4F, the preparation method is similar to that of BDP-pATS nanoagent. Briefly, pATS, aA2Ai, BDP and glyceryl trioctanoate were mixed to form a thin-film, which was then hydrated, finally to obtain an oil-in-water BDP-pATS-aA2Ai *via* passing the microemulsion through a microfluidizer. Subsequently, DLS measurements (Fig. 4G) were performed with results showing that BDP-pATS-aA2Ai revealed a *Z*-average of 139.0 ± 1.3 nm (PDI = 0.238 ± 0.011), which is further testified by TEM imaging displaying a monodispersed spherical structure (Fig. 4H). The drug-loading capacities were determined, with results of 3.8 ± 0.18% for pATS and 1.82 ± 0.13% for aA2Ai, respectively. Besides, the entrapment efficiency was determined to be 72.8 ± 3.7% for pATS and 83.6 ± 4.4% for aA2Ai, respectively. Furthermore, the stability of BDP-pATS-aA2Ai was also evaluated, with results of excellent storage at 4 °C within 30 days (Fig. 4I and J). Moreover, the release profile of A2Ai in BDP-pATS-aA2Ai was determined. As revealed in Supporting Information Fig. S9, BDP-pATS-aA2Ai also displayed a pH-dependent manner, with slightly reduced release rate compared with that of free aA2Ai. Subsequently, the cell viability of BDP-pATS-aA2Ai with or without light irradiation were also evaluated (Supporting Information Fig. S10), with similar patterns as that of BDP-pATS. These results demonstrated that BDP-pATS-aA2Ai nanoprodrug was well prepared, which can be testified for *in vivo* assays.

3.5. In vivo imaging, antitumor assay and immune evaluation

Before investigating the *in vivo* antitumor behavior, BDP-pATS-aA2Ai and BDP were firstly examined using near-infrared (NIR) *in vivo* fluorescence imaging in C57BL/6 mice bearing subcutaneous B16-F10 cells. To better illustrate their distribution, fluorescence imaging of *ex vivo* organs were shown in Fig. 5A. In general, BDP-pATS-aA2Ai revealed obvious higher fluorescence compared with BDP at each investigated time point, with both maximum values at 24 h and negligible fluorescence at 72 h. Concretely, BDP-pATS-aA2Ai mainly distributed in lungs and liver, whereas BDP in liver and kidneys. As for tumor accumulation capability, BDP-pATS-aA2Ai demonstrated excellent

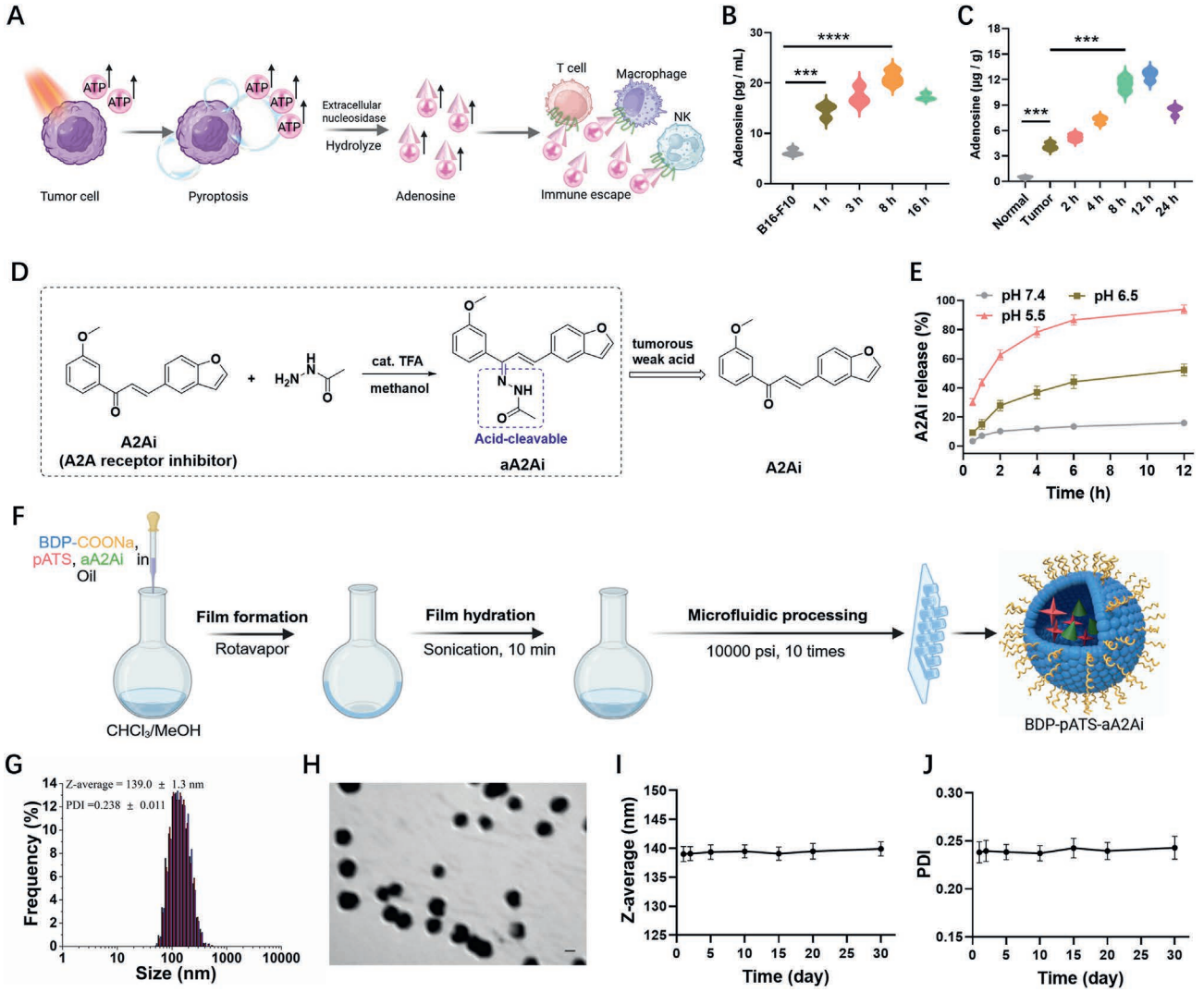

Figure 4 Preparation and characterization of BDP-pATS-aA2Ai nanoprodrug. (A) Schematic illustration of increased adenosine level to induce immune escape in tumor undergoing pyroptosis. (B, C) Adenosine level detection in the supernatant of B16-F10 cells and tumor tissues respectively using HPLC. (D) Synthesis of acid-activatable A2A receptor inhibitor prodrug aA2Ai. (E) A2Ai release profile in PBS at pH 7.4, 6.5 and 5.5, respectively. (F) Preparation process of BDP-pATS-aA2Ai by incorporating pATS and aA2Ai into the BDP core. (G) The DLS composite spectra obtained from three independent replicate experiments of BDP-pATS-aA2Ai: *Z*-average = 139.0 ± 1.3 nm; PDI = 0.238 ± 0.011. (H) TEM images of BDP-pATS-aA2Ai. Scale bar = 100 nm. (I, J) *Z*-average sizes and PDI values of BDP-pATS-aA2Ai within 30 days. ***$P < 0.001$ and ****$P < 0.0001$ *vs*. indicated. Data are expressed as mean ± SD ($n = 3$).

performance as compared to BDP at 24 h, which should benefit for its *in vivo* antitumor efficacy. Meanwhile, the corresponding fluorescence intensity values of major organs and tumors were listed in Fig. 5B and C.

In *in vivo* antitumor assay, we first evaluated the tumoricidal effect of A2Ai alone *via* blocking adenosine−A2AR pathway. As shown in Supporting Information Fig. S11, however, no significance was observed in tumor volumes between PBS and A2Ai (1 mg/kg, once a day for four times *via* tail vein injection) groups. Meanwhile, the body weight in both groups were steady with slight increasement within investigated times. These preliminary results indicated treatment with A2Ai alone under such doses had no significant effect on tumor suppression. Subsequently, the *in vivo* therapeutic effect of BDP-pATS-aA2Ai was examined by evaluating tumor growth on a subcutaneous B16-F10 tumor bearing mouse model. As the effect of A2Ai alone has been evaluated, herein mice were randomly divided into five groups, namely PBS, ATS, BDP + L, BDP-pATS + L and BDP-pATS-aA2Ai + L, respectively. The time schedule is listed in Fig. 6A, with tumor inoculation at Day 6, followed by indicated treatments. To achieve the effect of photo-controlled pyroptosis, one-time drug injection corresponding to two-time laser irradiation was performed, with the first irradiation for 3 min and the second irradiation for 7 min. During treatment period, all irradiation treated groups displayed steady increasement within investigated times (Fig. 6E). As displayed in Fig. 6D, tumors in PBS and ATS groups showed soaring growth profiles with similar changes, demonstrating ATS alone has little effects towards tumor inhibition. By contrast, the other three groups receiving irradiation verified remarkable inhibitory efficacy against tumor growth. Among them, BDP presented obvious antitumor activity toward tumors growth in the former days, which however finally failed to

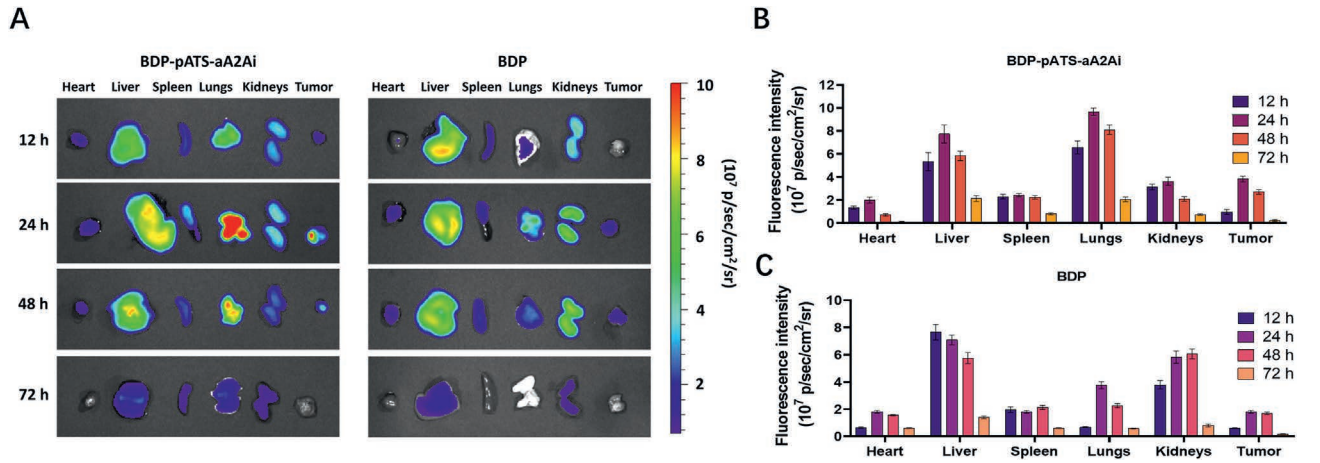

Figure 5 *In vivo* imaging using C57BL/6 mice bearing B16-F10 tumors after treatment with BDP-pATS-aA2Ai nanoprodrug and BDP, respectively. (A) Fluorescence images of major organs and tumors at different times. (B, C) The corresponding fluorescence intensity values of major organs and tumors. Data are expressed as mean ± SD ($n = 3$).

constrain rapidly growing tumors. BDP-pATS-aA2Ai + L proved the most potent antitumor efficacy with tumor growth inhibit rate (TGI) up to 99.4%, nearly complete tumor ablation of achieving curative level. As for BDP-pATS + L group, although three mice still bore untreated tumors, it still achieved high TGI values of 95.8%. However, no significance was observed between the last two groups (Fig. 6B and C). Still and all, the higher TGI value of BDP-pATS-aA2Ai may indicate its potential therapeutic superiority compared with BDP-pATS, which prompted us for further investigation.

Subsequently, we further investigated the immune response triggered by indicated treatments. $CD8^+$ T cells and $CD4^+$ T cells infiltration levels were determined using obtained tumors 12 days after treatment. As shown in Fig. 6F, H and I, BDP-pATS-aA2Ai + L group revealed potent $CD8^+$ T cells infiltration level of 14.6%, which is higher than 11.2% of BDP + L group, but exhibited no significance compared with 12.4% of BDP-pATS + L group. For comparison, both PBS and ATS groups showed lower cytotoxic T cells (CTLs) infiltration of 5.82% and 8.95%, respectively. In addition, $CD4^+$ T cell infiltration in these tumors revealed similar patterns, with maximum $CD4^+$ T cell infiltration level occurred in BDP-pATS-aA2Ai + L group of 32.5%, which has significant difference in comparison with 26.0% of BDP-pATS + L group. Besides, both groups manifested higher values than 20.8% of BDP + L group. PBS and ATS groups displayed lower values with negligible difference. Furthermore, immunofluorescence of $CD8^+$ and $CD4^+$ T cells in tumor tissues were also evaluated (Fig. 6G), wherein yellow and green fluorescence indicated $CD8^+$ T cells and $CD4^+$ T cells, which correlated well with the results of flow cytometric analysis. Hematoxylin and eosin (H&E) staining of the tumor tissues manifested that BDP-pATS + L and BDP-pATS-aA2Ai + L groups underwent significant tissue destruction compared with other groups (Fig. 6G), consisting well with their *in vivo* antitumor results.

As the significance was not observed towards tumor weight between groups of BDP-pATS + L and BDP-pATS-aA2Ai + L, the higher TGI value and immunological data indicated BDP-pATS-aA2Ai + L may bear superior performance. Herein, the percentage of survival assay was evaluated (Fig. 6J) as scheme illustrated in Fig. 6A, wherein BDP-pATS-aA2Ai + L group manifested the longest survival profile with survival rate of 80% at Day 38. For comparison, BDP-pATS + L group also exhibited substantially extended survival date at Day 38 with survival rate of 40%, which is obviously superior than BDP + L group with maximum survival date of only 22 days. For the other two groups, both encountered significantly decreased survival date, with maximum survival date of no more than 16 days. Taken together, these findings verified that BDP-pATS-aA2Ai + L exhibited superior efficacy compared with BDP-pATS + L, underscoring the importance of aA2Ai in enhancing antitumor therapy, which may further augment efficacy against tumor metastasis and recurrence.

3.6. Antitumor assay on bilateral tumor model and immune evaluation

Encouraged by aforementioned results, we further established a bilateral model using C57BL/6 mice bearing B16-F10 cells, to evaluate the efficacy against primary and distant tumors. The inoculation of bilateral tumors was performed as scheme illustrated in Fig. 7A, followed by subsequent immune analysis and tumor growth evaluation. As the general antitumor efficacy has been acquired in Fig. 5, we herein further focus on the last two groups, namely BDP-pATS + L and BDP-pATS-aA2Ai + L. Furthermore, as the efficacy in part 2.5 using only single time PDT (one-time injection and twice laser irradiation) was still undesirable, we herein adjust the scheme to twice PDT, namely twice injection and four-times laser irradiation, expecting potent efficacy not only to primary tumors, but also more significantly to distant tumors. As shown in Fig. 7B and G, the primary tumors were totally inhibited after treatment with twice PDT, with TGI values of 100% in both groups. For distant tumors, although both groups exhibited potent inhibition efficacy in the first 4 days, however, BDP-pATS + L started to rebound at Day 4, and gradually to be aggravated within 6−14 days with final TGI of 78.7%. By contrast, BDP-pATS-aA2Ai + L manifested excellent performance with TGI of 95.7%, which displayed a significant difference in comparison to BDP-pATS + L (Fig. 7C−G).

Furthermore, the immune response triggered by the indicated groups in distant tumors was also evaluated. Dendritic cells (DCs) represent the most potent APCs, working as a bridge between the former and the latter within the antitumor immunity. During the

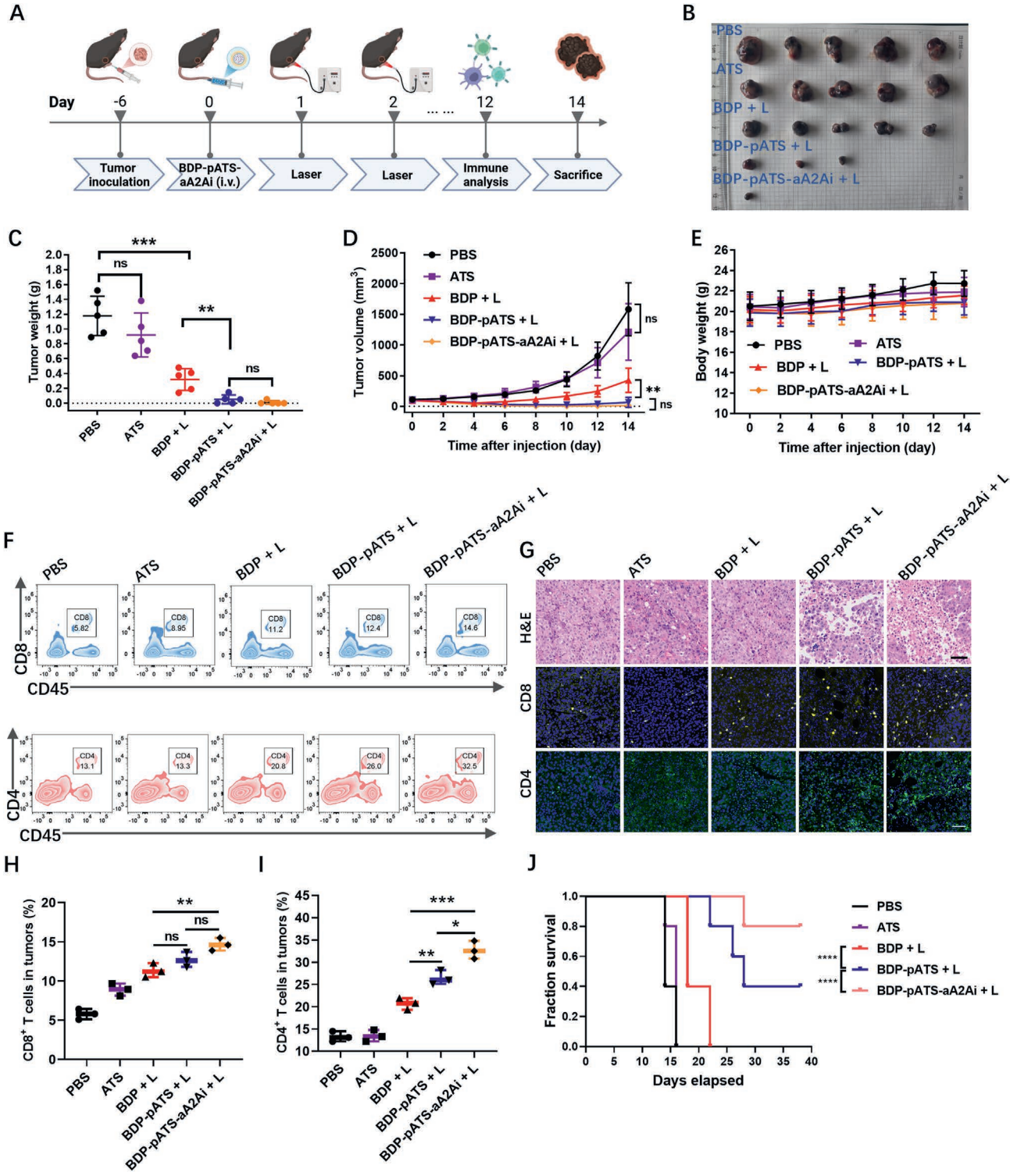

Figure 6 Antitumor assay and immune evaluation using C57BL/6 mice bearing B16-F10 tumors after indicated treatments. (A) Schematic illustration of *in vivo* antitumor regimen. BDP-pATS-aA2Ai nanodrug or BDP was i.v. administered *via* the tail vein. The mice were treated with a 660 nm laser for a total of 10 min (light power: 200 mW/cm^2; 3 min for the first irradiation and 7 min for the second irradiation). (B) Excised tumor images after 14 days (the missing sites represented the cured tumors). (C) The corresponding tumor weights in (B). (D) Change curves of tumor volume within investigated time. (E) Change curves of body weight. (F) Flow cytometric plots of $CD8^+$ and $CD4^+$ T cells in tumors after indicated treatments. (G) H&E staining of tumor tissues in indicated groups. Scale bar = 60 μm. Immunofluorescence images of $CD8^+$ and $CD4^+$ T cells in tumor tissues. Yellow and green fluorescence indicate $CD8^+$ T cells and $CD4^+$ T cells, respectively. Scale bar = 50 μm. (H, I) Quantification of $CD8^+$ and $CD4^+$ T cells in (F) ($n = 3$). (J) Kaplan−Meier survival curves of mice after various treatments. Statistical analysis was performed by Student's *t*-test. $^*P < 0.05$, $^{**}P < 0.01$, $^{***}P < 0.001$, $^{****}P < 0.0001$ *vs.* indicated, and ns represents no significant difference.

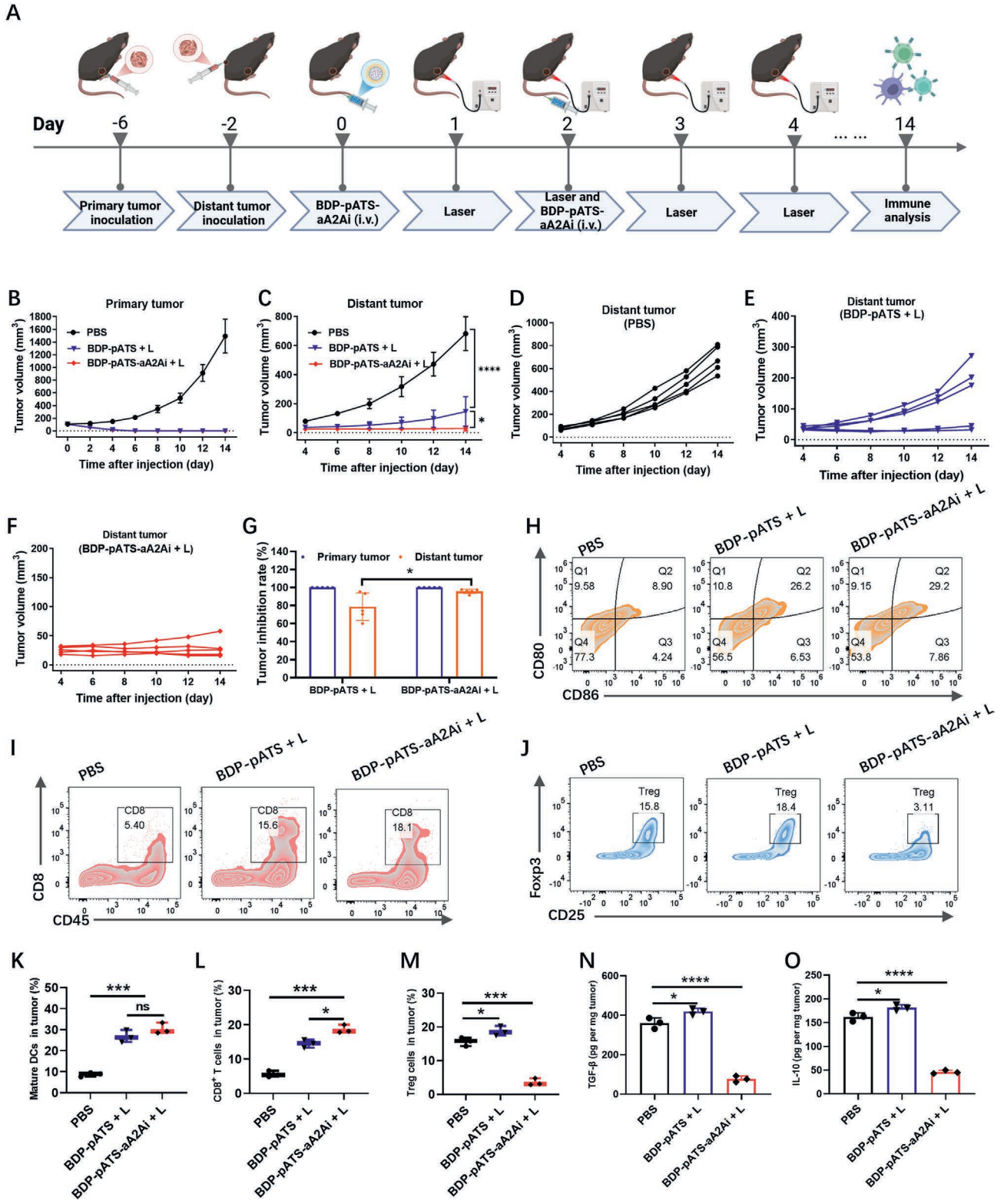

Figure 7 Antitumor assay on bilateral tumor model and immune evaluation. (A) Schematic illustration of a bilateral B16-F10 tumor model and its corresponding treatment schedule. (B, C) Change curves of primary and distant tumor volume within 14 days. (D−F) Individual tumor growth curves of distant tumor in B16-F10 tumor bearing mice after receiving indicated treatments ($n = 5$). (G) Tumor growth inhibition rate of primary and distant tumor. (H−J) Flow cytometric plots of mature DCs, $CD8^+$ T cells and Treg cells in distant tumors, respectively. (K−M) Quantification of mature DCs, $CD8^+$ T cells and Treg cells in (H−J), respectively ($n = 3$). (N, O) Expression levels of TGF-β and IL-10 in tumors after indicated treatments ($n = 3$). Statistical analysis was performed by Student's *t*-test. $^*P < 0.05$, $^{***}P < 0.001$, $^{****}P < 0.0001$ *vs.* indicated, and ns represents no significant difference.

pyroptosis process, naïve DCs are stimulated by damage-associated molecular patterns (DAMPs) to form mature DCs, which further process and present tumor associated antigens (TAAs) to T cells, enhancing the infiltration of CTLs in the TME, ultimately achieving specific immune tumoricidal effects. Therefore, DC maturation was determined *via* analyzing the tumors collected from the indicated groups. As demonstrated in Fig. 7H and K, BDP-pATS-aA2Ai + L and BDP-pATS + L treatment groups exhibited substantially elevated levels of mature DCs, with increases of 3.28- and 2.94-fold respectively, relative to the PBS group. Besides, groups of BDP-pATS-aA2Ai + L and BDP-pATS + L revealed DCs maturation of 29.2% and 26.2% respectively, however, these two groups exhibited no significance. Besides, the immunoactivation efficacy was further investigated on CTLs and Treg cells, which are target cells of A2Ai with high expression of A2AR. For $CD8^+$ T cells, BDP-pATS-aA2Ai + L group was the most potent of 18.1%, which is higher than that in BDP-pATS + L of 15.6% and PBS group of 5.4%, respectively (Fig. 7I and L). Although no significant difference in $CD8^+$ T cell levels was observed between the two groups (Fig. 6H), in distant tumors specifically, BDP-pATS-aA2Ai + L demonstrated a statistically significant increase compared to BDP-pATS + L. For Treg cells (Fig. 7J and M), BDP-pATS-aA2Ai + L displayed Treg level of 3.11%, which is remarkably lower than that in BDP-pATS + L (18.4%) and PBS group (15.8%). Furthermore, immunosuppressive cytokines secreted by Treg cells such as TGF-β and IL-10 were also determined. As shown in Fig. 7N and O, the contents of TGF-β and IL-10 in BDP-pATS + L group were higher than that in PBS group, whereas BDP-pATS-aA2Ai + L group remarkably decreased their levels, further indicating the effective blocking against adenosine−A2AR pathway. Collectively, these data manifested that BDP-pATS-aA2Ai + L can simultaneously ignite PDT efficacy, reinvigorate potent CTLs infiltration and significantly restrain the immunosuppressive Treg cells, which all contributed to the desirable antitumor performance.

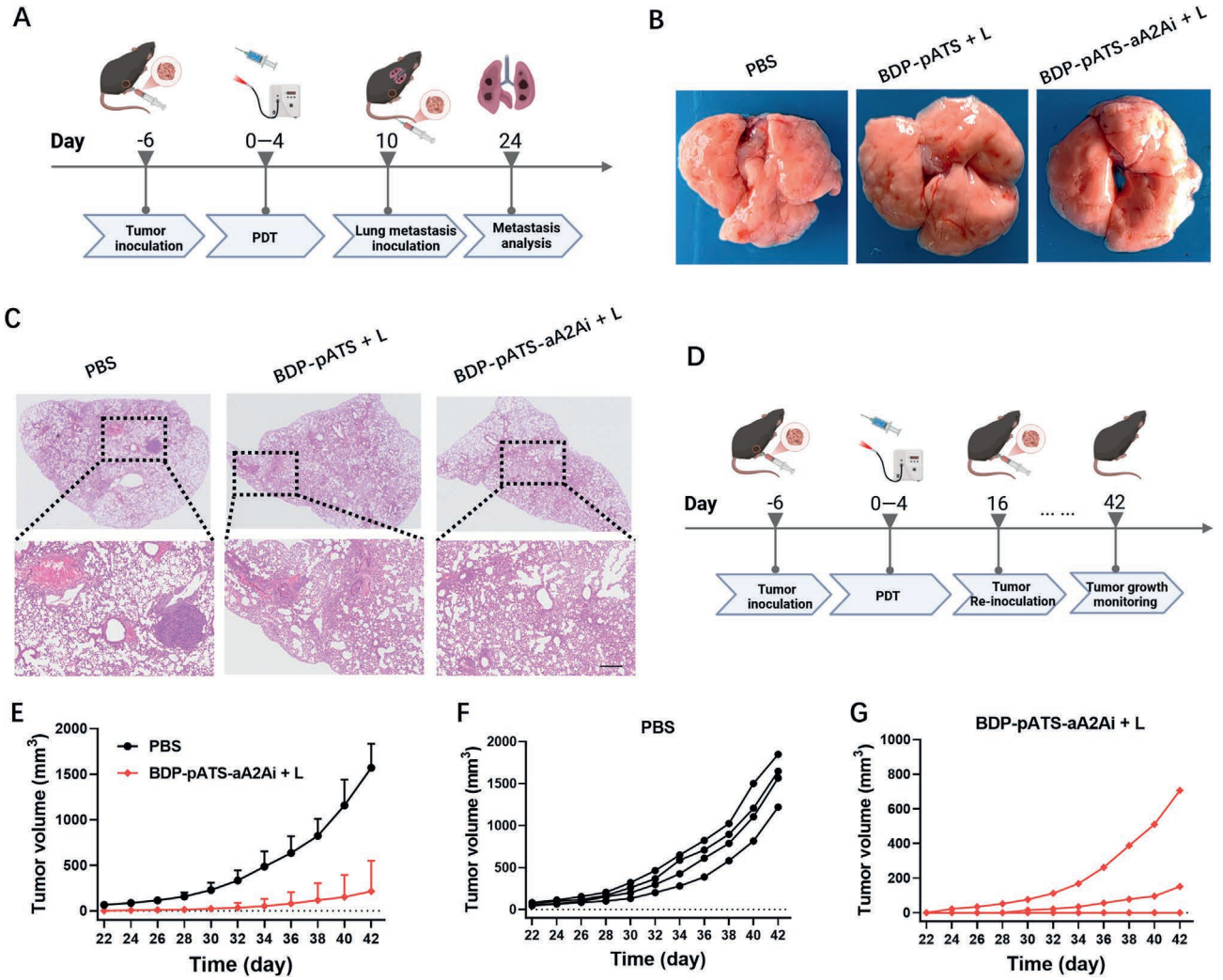

Figure 8 Antitumor effects toward lung metastasis and tumor recurrence. (A) Schematic illustration of B16-F10 cell bearing lung metastasis mouse model. (B) Representative images of lungs after indicated treatments. (C) Representative images of H&E staining of lung tissues in PBS, BDP-pATS + L and BDP-pATS-aA2Ai + L treated groups, respectively. Scale bar = 50 μm. (D) Schematic illustration of B16-F10 cell bearing mouse model towards tumor recurrence. (E) Change curves of recurrent tumor volume. (F, G) Individual tumor growth curves of recurrence tumor in B16-F10 cell bearing mice after receiving indicated treatments (n = 4). For lung metastasis and tumor recurrence assays, twice PDT scheme was performed, namely with two injections and four-times laser irradiation (200 mW/cm^2, a total of 20 min).

3.7. Antitumor effects towards lungs metastasis and tumor recurrence

Lung metastasis is a typical type among patients with distant tumor metastasis. Herein, we established a melanoma lung metastasis model to evaluate the antitumor efficacy evoked by BDP-pATS-aA2Ai + L treatment. As shown in Fig. 8A, C57BL/6 mice were injected with B16-F10 cells (3×10^5 cells/mouse) *via* the tail vein on Day 10 after PDT treatment. Afterwards, lung tissues were collected on Day 24 and used for H&E staining to evaluate the behavior of lung metastasis. As revealed in Fig. 8C, BDP-pATS-aA2Ai + L treatment obviously attenuated the number of lung tumor nodes compared with both PBS and BDP-pATS + L groups, proving its desirable antitumor metastatic capability. Meanwhile, the images of the isolated lung were also provided in Fig. 8B. In addition, the body weights were steady without pathological changes in each group (Supporting Information Fig. S12). Taken together, BDP-pATS-aA2Ai + L treatment effectively restrained lung metastasis of melanoma in B16-F10 bearing living mice.

In addition to metastasis, tumor recurrence also accounts for the main reasons underlying cancer-related deaths. A successful antitumor therapeutic platform should not only demonstrate robust tumoricidal activity against established primary and metastatic tumors, but also can further sustain immunological memory to provide long-term protection against tumor recurrence. Encouraged by the aforementioned results, we subsequently established a tumor rechallenge model manipulating BDP-pATS-aA2Ai + L against melanoma recurrence. As illustrated in Fig. 8D, B16-F10 cells (3×10^5 cells/mouse) were inoculated on Day 6, followed by twice PDT treatment. After the first tumor inoculation, mice achieving complete tumors ablation were rechallenged with the second subcutaneous injection of B16-F10 cells (2×10^5 cells/mouse) on Day 16. As exhibited in Fig. 8E−G, 50% tumor-free occurrence (2 out of 4 mice) were observed in mice previously treated with BDP-pATS-aA2Ai + L from Day 16 to Day 42, which was in sharp contrast to rapid tumor growth in PBS-treated mice. Concretely, tumor recurrence was first detected at Day 24 with minor tumor volume, followed by rapid growth from Day 32 to Day 42. Another tumor maintained growth quiescence until Day 30, after which progressive tumor expansion was observed. Of particular note, two mice remained completely recurrence-free throughout the entire observation period. These results verified the durable and potent antitumor capability against B16-F10 cell bearing recurrence tumor *via* BDP-pATS-aA2Ai-mediated photoimmunotherapy. Collectively, the immune efficacy of BDP-pATS-aA2Ai, generated by PDT-based immunogenic pyroptosis synergistic with adenosine−A2AR blocking, can noticeably inhibit the metastatic and recurrent tumors in living C57BL/6 mice.

4. Conclusions

This work constructed a novel multifunctional nanoprodrug system, incorporating photo-controlled pyroptosis and acid-activatable adenosine−A2AR interruption into a single nanotherapeutic platform, serving as the synergistic photoimmunotherapy and immunometabolic therapeutics. *In vitro* and *in vivo* results consistently manifested that BDP-pATS-aA2Ai-mediated synergistic therapeutics can not only potentiate tumor immunogenicity *via* PDT-based pyroptosis, but also counterbalance immunosuppressive TME *via* inhibiting adenosine−A2AR pathway, finally facilitating potent CTLs infiltration and decreasing the immunosuppressive Treg cells in TME. Such a synergistic therapeutic platform of BDP-pATS-aA2Ai completely eradicated primary tumors, and also effectively restrained pulmonary metastasis and reinoculation-induced tumor recurrence, which barely can be accomplished by mono-immunotherapy or traditional photodynamic therapy.

There are several limitations existing within our study. First, although desirable results were manifested on *in vivo* antitumor models, this work preliminarily evaluated the tumor suppression efficacy towards lung metastatic and tumor recurrence, wherein the systemic immunological memory indicators should also be analyzed in our future research. Second, the generalizability of this platform across different tumor types needs experimental validation. Last, whether our newly discovered application of artesunate, serving as a novel epigenetic drug, has widespread application also demands further research. Despite these limitations, our work establishes a novel therapeutic paradigm that combines photoimmunotherapy with immunometabolic modulation, offering a new perspective for melanoma treatment.

Acknowledgements

This work was supported by the National Natural Science Foundation of China (Nos. 82303787 and 82073385), Postdoctoral Fellowship Program of CPSF (GZB20230522, China), China Postdoctoral Science Foundation (2020M671234), and Science and Technology Commission of Shanghai Municipality (23S21900800, China).

Author contributions

Zhiliang Yu and Hong Wang conceived and designed this project. Zhiliang Yu performed all chemical experiments and composed the manuscript. Zhiliang Yu and Hong Wang performed the *in vitro* and *in vivo* experiments. Zongguang Tai, Zhongjian Chen and Quangang Zhu supervised this work. Zhiliang Yu, Zhongjian Chen and Quangang Zhu obtained financial supports. Zongguang Tai, Zhongjian Chen, Quangang Zhu, Qin Yu, Fengze Miao and Rongrong Chai provided resources and revised the manuscript. All authors have approved the final version of the manuscript.

Conflicts of interest

The authors declare no conflicts of interest.

Appendix A. Supporting information

Supporting information to this article can be found online at https://doi.org/10.1016/j.apsb.2026.01.024.

References

1. Kraehenbuehl L, Weng CH, Eghbali S, Wolchok JD, Merghoub T. Enhancing immunotherapy in cancer by targeting emerging immunomodulatory pathways. *Nat Rev Clin Oncol* 2022;**19**:37−50.
2. Lin MJ, Svensson-Arvelund J, Lubitz GS, Marabelle A, Melero I, Brown BD, et al. Cancer vaccines: the next immunotherapy frontier. *Nat Cancer* 2022;**3**:911−26.

3. Huang AC, Zappasodi R. A decade of checkpoint blockade immunotherapy in melanoma: understanding the molecular basis for immune sensitivity and resistance. *Nat Immunol* 2022;**23**:660−70.
4. Graciotti M, Kandalaft LE. Vaccines for cancer prevention: exploring opportunities and navigating challenges. *Nat Rev Drug Discov* 2024;**24**:134−50.
5. Weiss F, Lauffenburger D, Friedl P. Towards targeting of shared mechanisms of cancer metastasis and therapy resistance. *Nat Rev Cancer* 2022;**22**:157−73.
6. O'Sullivan Coyne G, Madan RA, Gulley JL. Nivolumab: promising survival signal coupled with limited toxicity raises expectations. *J Clin Oncol* 2014;**32**:986−8.
7. Reck M, Rodríguez-Abreu D, Robinson AG, Hui R, Csőszi T, Fülöp A, et al. Pembrolizumab versus chemotherapy for PD-L1-positive non-small-cell lung cancer. *N Engl J Med* 2016;**375**:1823−33.
8. Larkin J, Chiarion-Sileni V, Gonzalez R, Grob JJ, Cowey CL, Lao CD, et al. Combined nivolumab and ipilimumab or monotherapy in untreated melanoma. *N Engl J Med* 2015;**373**:23−34.
9. Bellmunt J, de Wit R, Vaughn DJ, Fradet Y, Lee J-L, Fong L, et al. Pembrolizumab as second-line therapy for advanced urothelial carcinoma. *N Engl J Med* 2017;**376**:1015−26.
10. Liang Y, Zhang JG, Wang JJ, Yang YH, Tan XY, Li SG, et al. Restoring tumor cell immunogenicity through ion-assisted mRNA domestication for enhanced *in situ* cancer vaccination effect. *Adv Sci* 2025;**12**:2500825.
11. Zhang YJ, Wu XH, Wang KY, Tang YH, Lu XX, Sun FS, et al. Simultaneous reversal of T lymphocytes and cancer cells metabolism *via* a biomimetic heavy-atom-free photosensitizers-based combination therapies to boost cancer photoimmunotherapy. *Adv Sci* 2025;**12**:2416143.
12. Viel S, Vivier E, Walzer T, Marçais A. Targeting metabolic dysfunction of CD8 T cells and natural killer cells in cancer. *Nat Rev Drug Discov* 2024;**24**:190−208.
13. Jiang XM, Lin WB. Innate immune activation with multifunctional nanoparticles for cancer immunotherapy. *Angew Chem Int Ed* 2025;**64**:e202423280.
14. Gong N, Alameh M-G, El-Mayta R, Xue L, Weissman D, Mitchell MJ. Enhancing *in situ* cancer vaccines using delivery technologies. *Nat Rev Drug Discov* 2024;**23**:607−25.
15. Jin XK, Zhang SK, Zhang SM, Liang JL, Yan X, Lin YT, et al. Disrupting intracellular homeostasis by copper-based nanoinducer with multiple enzyme-mimicking activities to induce disulfidptosis-enhanced pyroptosis for tumor immunotherapy. *Adv Mater* 2024;**37**:2410957.
16. Liu X, Xia SY, Zhang ZB, Wu H, Lieberman J. Channelling inflammation: gasdermins in physiology and disease. *Nat Rev Drug Discov* 2021;**20**:384−405.
17. Broz P, Pelegrín P, Shao F. The gasdermins, a protein family executing cell death and inflammation. *Nat Rev Immunol* 2019;**20**:143−57.
18. Li WS, Li HY, Jiang GW, Yang L, Nie HF, Lin CT, et al. Creating single atomic coordination for hypoxia-resistant pyroptosis nanoinducer to boost anti-tumor immunotherapy. *Adv Mater* 2025;**37**:2414697.
19. Wang SM, Ma D, Yang MH, Zhang Y, Wang SF, Zhou WH. Arsenic trioxide-based nanoparticles for enhanced chemotherapy by activating pyroptosis. *Acta Pharm Sin B* 2025;**15**:6001−18.
20. Huang YL, Wang CT, Chen YH, Wang DB, Yao DF. Nanomedicine-induced pyroptosis for anti-tumor immunotherapy: mechanism analysis and application prospects. *Acta Pharm Sin B* 2025;**15**:3487−510.
21. Glorieux C, Liu S, Trachootham D, Huang P. Targeting ROS in cancer: rationale and strategies. *Nat Rev Drug Discov* 2024;**23**:583−606.
22. Wang H, Jing GX, Niu JT, Yang L, Li YY, Gao Y, et al. A mitochondria-anchored supramolecular photosensitizer as a pyroptosis inducer for potent photodynamic therapy and enhanced antitumor immunity. *J Nanobiotechnol* 2022;**20**:513.
23. Zhang XY, Bao LL, Yu ZL, Miao FZ, Li LS, Cui Z, et al. Nano-engineered M1 macrophages enhance photodynamic therapy of melanoma through oxygen production and subsequent antitumor immunity. *Chem Eng J* 2024;**487**:150153.
24. Yu ZL, Wang H, Chen ZJ, Dong XC, Zhao WL, Shi YL, et al. Discovery of an amino acid-modified near-infrared aza-BODIPY photosensitizer as an immune initiator for potent photodynamic therapy in melanoma. *J Med Chem* 2022;**65**:3616−31.
25. Donohoe C, Senge MO, Arnaut LG, Gomes-da-Silva LC. Cell death in photodynamic therapy: from oxidative stress to anti-tumor immunity. *Biochim Biophys Acta Rev Cancer* 2019;**1872**:188308.
26. Zhang ZB, Zhang Y, Xia SY, Kong Q, Li SY, Liu X, et al. Gasdermin E suppresses tumour growth by activating anti-tumour immunity. *Nature* 2020;**579**:415−20.
27. Yi ZG, Qin XJ, Zhang L, Chen H, Song TL, Luo ZC, et al. Mitochondria-targeting type-I photodrug: harnessing caspase-3 activity for pyroptotic oncotherapy. *J Am Chem Soc* 2024;**146**:9413−21.
28. Wang YP, Gao WQ, Shi XY, Ding JJ, Liu W, He HB, et al. Chemotherapy drugs induce pyroptosis through caspase-3 cleavage of a gasdermin. *Nature* 2017;**547**:99−103.
29. Hogg SJ, Beavis PA, Dawson MA, Johnstone RW. Targeting the epigenetic regulation of antitumour immunity. *Nat Rev Drug Discov* 2020;**19**:776−800.
30. Millán-Zambrano G, Burton A, Bannister AJ, Schneider R. Histone post-translational modifications—cause and consequence of genome function. *Nat Rev Genet* 2022;**23**:563−80.
31. Liu YC, Kwon J, Fabiani E, Xiao Z, Liu YV, Follo MY, et al. Demethylation and up-regulation of an oncogene after hypomethylating therapy. *N Engl J Med* 2022;**386**:1998−2010.
32. Bertoli RM, Chung YJ, Difilippantonio MJ, Wokasch A, Marasco MRB, Klimaszewski H, et al. The DNA methyltransferase inhibitor 5-aza-4′-thio-2′-deoxycytidine induces C>G transversions and acute lymphoid leukemia development. *Cancer Res* 2024;**84**:2518−32.
33. Wang H, Gao ZY, Jiao D, Zhang YF, Zhang JT, Wang TJ, et al. A microenvironment dual-responsive nano-drug equipped with PD-L1 blocking peptide triggers immunogenic pyroptosis for prostate cancer self-synergistic immunotherapy. *Adv Funct Mater* 2023;**33**:2214499.
34. Wu CR, Wang H, Niu JT, Wei BG, Gao Y, Li YY, et al. Combination of an LDH-based platform with microRNA for the treatment of myocardial ischemia−reperfusion injury by pyroptosis inhibition *via* the CaSR/PLCγ1/IP3R pathway. *Chem Eng J* 2025;**508**:160833.
35. Wang H, Yu ZL, Jing GX, Wang ZJ, Niu JT, Qian YC, et al. Etoposide-loaded layered double hydroxide achieves the best of both worlds: simultaneous breast carcinoma inhibition and embryo protection *via* selectively regulating Caspase 3-GSDME pyroptosis pathway. *Chem Eng J* 2024;**484**:149485.
36. Wang WS, Zhu CH, Zhang B, Feng Y, Zhang Y, Li JB. Self-assembled nano-PROTAC enables near-infrared photodynamic proteolysis for cancer therapy. *J Am Chem Soc* 2023;**145**:16642−9.
37. Chen YC, Xiong T, Peng Q, Du JJ, Sun W, Fan JL, et al. Self-reporting photodynamic nanobody conjugate for precise and sustainable large-volume tumor treatment. *Nat Commun* 2024;**15**:6935.
38. Wan JQ, Ren LL, Li XY, He SS, Fu Y, Xu PR, et al. Photoactivatable nanoagonists chemically programmed for pharmacokinetic tuning and *in situ* cancer vaccination. *Proc Natl Acad Sci U S A* 2023;**120**:e2210385120.
39. Klöcker N, Weissenboeck FP, van Dülmen M, Špaček P, Hüwel S, Rentmeister A. Photocaged 5′ cap analogues for optical control of mRNA translation in cells. *Nat Chem* 2022;**14**:905−13.
40. Liu L, Zhang D, Johnson M, Devaraj NK. Light-activated tetrazines enable precision live-cell bioorthogonal chemistry. *Nat Chem* 2022;**14**:1078−85.
41. Wilson DS, Dalmasso G, Wang L, Sitaraman SV, Merlin D, Murthy N. Orally delivered thioketal nanoparticles loaded with TNF-α−siRNA target inflammation and inhibit gene expression in the intestines. *Nat Mater* 2010;**9**:923−8.
42. Liu B, Thayumanavan S. Mechanistic investigation on oxidative degradation of ROS-responsive thioacetal/thioketal moieties and their implications. *Cell Rep Phys Sci* 2020;**1**:100271.

43. Baryakova TH, Pogostin BH, Langer R, McHugh KJ. Overcoming barriers to patient adherence: the case for developing innovative drug delivery systems. *Nat Rev Drug Discov* 2023;**22**:387−409.
44. Hou WX, Lou JWH, Bu JC, Chang EL, Ding LL, Valic M, et al. A nanoemulsion with a porphyrin shell for cancer theranostics. *Angew Chem Int Ed* 2019;**58**:14974−8.
45. Yu ZL, Zhou JL, Ji X, Lin GY, Xu S, Dong XC, et al. Discovery of a monoiodo aza-BODIPY near-infrared photosensitizer: *in vitro* and *in vivo* evaluation for photodynamic therapy. *J Med Chem* 2020;**63**: 9950−64.
46. Liu C, Ji X, Yu ZL, Zhang SH, Zhang R, Zhao WL, et al. Discovery of subcellular-targeted aza-BODIPY photosensitizers for efficient photodynamic antitumor therapy. *J Med Chem* 2023;**66**: 7205−20.
47. Allard B, Allard D, Buisseret L, Stagg J. The adenosine pathway in immuno-oncology. *Nat Rev Clin Oncol* 2020;**17**:611−29.
48. Zhang YY, Jin WW, Deng ZC, Gao BW, Zhu YY, Fu JL, et al. Metabolic reprogramming nanomedicine potentiates colon cancer sonodynamic immunotherapy by inhibiting the CD39/CD73/ADO pathway. *Acta Pharm Sin B* 2025;**15**:2655−72.
49. Bantug GR, Hess C. The immunometabolic ecosystem in cancer. *Nat Immunol* 2023;**24**:2008−20.
50. Zeng SM, Qu WQ, Sun YL, Chen KW, Zhao K, Yan JH, et al. MnO_2-assisted photosynthetic bacteria interfering with the adenosine−A2AR metabolic pathway to enhance tumor photothermal immunotherapy. *ACS Nano* 2025;**19**:7962−80.
51. Liu YQ, Liu Y, Xu DL, Zang J, Zheng X, Zhao YG, et al. Targeting the negative feedback of adenosine−A2AR metabolic pathway by a tailored nanoinhibitor for photothermal immunotherapy. *Adv Sci* 2022; **9**:2104182.
52. Li X, Wenes M, Romero P, Huang SC, Fendt SM, Ho PC. Navigating metabolic pathways to enhance antitumour immunity and immunotherapy. *Nat Rev Clin Oncol* 2019;**16**:425−41.
53. Zhao YT, Xie ZZ, Deng YY, Huang AJ, He YL, Wen B, et al. Photothermal nanobomb blocking metabolic adenosine−A2AR potentiates infiltration and activity of T cells for robust antitumor immunotherapy. *Chem Eng J* 2022;**450**:138139.
54. Xu C, Jiang YY, Huang JS, Huang JG, Pu KY. Second near-infrared light-activatable polymeric nanoantagonist for photothermal immunometabolic cancer therapy. *Adv Mater* 2021;**33**:2101410.
55. Zhang RJ, Rao QR, Jiang XQ, Ye N, Li N, Du HL, et al. Exploring the immunomodulatory properties of red onion (Allium cepa L.) skin: isolation, structural elucidation, and bioactivity study of novel onion chalcones targeting the A2A adenosine receptor. *J Agric Food Chem* 2023;**71**:17046−55.
56. Li YQ, Wang W, Li AX, Huang W, Chen SM, Han F, et al. Dihydroartemisinin induces pyroptosis by promoting the AIM2/caspase-3/DFNA5 axis in breast cancer cells. *Chem Biol Interact* 2021;**340**: 109434.
57. O'Brien Laramy M, Foley DA, Pak RH, Lewis JA, McKinney E, Egan PM, et al. Chemistry, manufacturing and controls strategies for using novel excipients in lipid nanoparticles. *Nat Nanotechnol* 2025; **20**:331−44.
58. Lin YT, Meng R, Zhang SM, Zhou H, Chen H, Liang JL, et al. Acid-responsive biocompatible hydrogel modulating tumor DNA self-repair collaborated with chemotherapy for boosting STING pathway-associated immunotherapy. *Nano Lett* 2025;**25**:3670−80.
59. Jiang Z, Hu YT, Guo SY, Li YX, Zhao DD, Wei LY, et al. Development of novel *N*-acylhydrazone derivatives with high anti-obesity activity and improved safety by exploring the pharmaceutical properties of aldehyde group. *J Med Chem* 2024;**67**:12439−58.
60. Beck A, Goetsch L, Dumontet C, Corvaïa N. Strategies and challenges for the next generation of antibody−drug conjugates. *Nat Rev Drug Discov* 2017;**16**:315−37.
61. Carter PJ, Lazar GA. Next generation antibody drugs: pursuit of the 'high-hanging fruit'. *Nat Rev Drug Discov* 2017;**17**:197−223.